A SEARCH FOR SUPERSYMMETRY IN EVENTS WITH A Z BOSON, JETS, AND MISSING TRANSVERSE ENERGY IN $p-p$ COLLISIONS WITH $\sqrt{s}$=13 TEV WITH THE ATLAS DETECTOR

TOVA RAY HOLMES

Physics Department
University of California, Berkeley

August 2016 – version 1.0

ABSTRACT

PUBLICATIONS

Some ideas and figures have appeared previously in the following publications:

Put your publications from the thesis here. The packages `multibib` or `bibtopic` etc. can be used to handle multiple different bibliographies in your document.

ACKNOWLEDGEMENTS

Put your acknowledgements here.

CONTENTS

LIST OF FIGURES

LIST OF TABLES

LISTINGS

ACRONYMS

LHC Large Hadron Collider

IBL Insertable B-Layer

MS Muon Spectrometer

ID Inner Detector

SCT Silicon Microstrip Tracker

TRT Transition Radiation Tracker

NN Neural Network

CCA Connected Component Analysis

ToT Time Over Threshold

MDT Monitored Drift Tube

CSC Cathode-Strip Chamber

RPC Resistive Plate Chamber

TGC Thin Gap Chamber

MC Monte Carlo simulation

SM Standard Model

BSM Beyond the Standard Model

SUSY Supersymmetry

QCD Quantum Chromodynamics

PDF Parton Distribution Function

DM Dark Matter

NLO+NLL Next-to-Leading-Logarithmic Accuracy

AOD Analysis Object Data

SR Signal Region

VR Validation Region

CR Control Region

FS Flavor Symmetric

Part I

INTRODUCTION

The centerpiece of this thesis is a search for Supersymmetry, but it also includes all the scaffolding and background necessary to understand the search. An overview of the Large Hadron Collider (LHC) and the ATLAS Detector are presented along with the theory that motivates the search.

1 INTRODUCTION

The pages that follow detail the author's work on the ATLAS experiment from 2011 through 2016, focusing on an analysis of 13*TeV* proton-proton collisions at the LHC looking for Supersymmetry with the ATLAS Detector.

CHAPTER 2 outlines the Standard Model of Particle Physics and the benefits of extending it to include Supersymmetry, then continues to describe the motivation behind searching for this particular model.

CHAPTER 3 describes the LHC and its operation.

CHAPTER 4 contains descriptions of the many pieces of the ATLAS detector, and how they serve to detect particles coming from LHC collisions.

CHAPTER 5 presents a neural network designed to improve tracking in the ATLAS Pixel Detector, and describes the benefits of its implementation.

Part II

THEORY AND MOTIVATION

This section describes the theoretical foundation for the analysis presented in Part iv. It includes an overview of the Standard Model, including its phenomenology in a $p-p$ collider. The theory of Supersymmetry is explained, and the motivation for extending the Standard Model to include it is presented. In addition, this section includes an explanation of Monte Carlo generators and details about the specific form of Supersymmetry searched for in this analysis.

2 THEORY AND MOTIVATION

The Standard Model (SM) of particle physics represents all particles and interactions currently understood by the particle physics community. It is formulated using the principles of Quantum Field Theory, with the constraints of several symmetries and physical requirements to determine the rules for allowed interactions. [22] Developed in the 1960s and 70s, it has been immensely successful at predicting additional particles, and has held up to many high-precision tests. Despite this success, it has several shortcomings which point to its incompleteness. Though the SM is likely correct at the energies thus far probed, it may be missing key components that become more important at higher energies. Models supplementing the SM with additional particles and interactions are referred to as Beyond the Standard Model (BSM) theories.

One possible extension of the SM is Supersymmetry (SUSY), a theory which applies an additional symmetry between bosons and fermions to the SM, creating a spectrum of SUSY particles (sparticles) which interact with the particles of the SM. This theory motivates the search performed in Part iv, and its theoretical appeals are discussed in this section, along with specific simplified models considered in the search.

2.1 THE STANDARD MODEL

The SM of particle physics describes the interactions of all of the particles currently known to exist, and consists of both matter particles and force carriers. This model has been unprecedentedly successful in predicting new particles and phenomena, including the prediction of the Higgs particle almost 50 years before its discovery in 2012, which completed the SM. This section describes the components of the SM and how they interact, focusing on the environment of the LHC.

The particles of the SM are divided into two categories: fermions and bosons. The fermions comprise all the matter described by the SM, and are spin-$\frac{1}{2}$ particles. The bosons, integer-spin particles, are the force carriers. They provide a mechanism to explain three of the four forces known to particle physics, with gravity still lacking a quantum formalization. The Higgs boson, the only spin-0 particle in the SM, provides a mechanism for giving mass to the other particles. The full SM, with the addition of the hypothetical graviton, is presented in Figure 1.

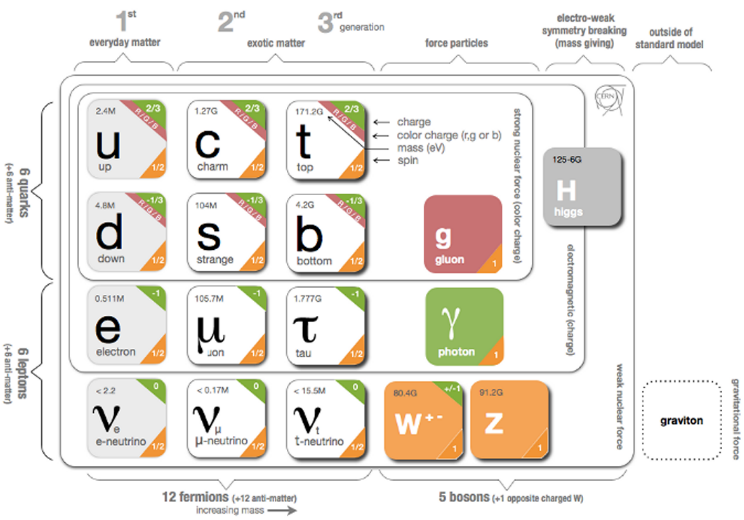

Figure 1: The Standard Model of particle physics, containing all known bosons and fermions, with the addition of the hypothetical graviton. [32]

2.1.1 *Matter*

The matter described by the SM is made up of fermions, spin-$\frac{1}{2}$ particles which can be broken into two groups, quarks and leptons. The leptons all interact weakly, while the quarks additionally interact strongly.

2.1.1.1 *Leptons*

Leptons, as seen in the bottom left of Figure 1, come in three generations, each labeled by a flavor: electron, muon, and tau. In the case of the massive leptons, these flavors are mass eigenstates, and the generations are placed in an order based on increasing mass. Each massive lepton is negatively charged and has a positively charged anti-particle.

The three neutrinos come in the same flavors as the massive leptons, but these flavor eigenstates do not correspond exactly to mass eigenstates. As a consequence, neutrinos oscillate between flavors as they propagate through space. These oscillations are the only evidence of neutrino mass, which is bound from below by the mass splittings determined from the oscillation. Though it is still uncertain if the masses of the neutrinos follow the same hierarchy as the massive leptons, that expected ordering is slightly preferred over the inverted hierarchy. [35]

Unlike the massive leptons, the neutrinos are uncharged, and it is not yet known whether each neutrino has a separate anti-particle, or if it is its own antiparticle. Because they are uncharged, they can only interact weakly, making them extremely difficult to detect. In the AT-

LAS detector, neutrinos pass through all layers undetected, and their presence can only be inferred from the non-conservation of momentum that results in the observed particles. As a consequence of their ability to evade detection, neutrinos are the least understood particles of the SM.

The SM conserves lepton number, L, which is defined as the number of leptons minus the number of anti-leptons in a state. While this conservation is not theoretically required, its violation has not yet been observed. As a consequence of this conservation, the lightest massive lepton, the electron, is stable.

2.1.1.2 *Quarks*

Quarks, as seen in the top left of Figure 1, are also charged particles that interact weakly, but are differentiated from the leptons by their strong interactions. They are also organized in three generations ordered by mass, and come in pairs of "up-type" and "down-type" quarks, named after the lightest generation. Though the up quark is lighter than the down, that rule is reversed in the subsequent two generations. Up-type quarks are charged $+\frac{2}{3}$, while the down-type quarks are charged $-\frac{1}{3}$. Quarks are also charged under the strong interaction, whose three charges are often characterized by colors: red, green, and blue. Each quark has an anti-particle with the opposite charges.

These fractional charges and individual colors are never seen in nature because of the requirement (discussed further in Section 2.1.2.2) that stable particle states be color-neutral. To accomplish this, quarks can create two-particle bound states called *mesons* consisting of one quark and one anti-quark with the same color charge or three-particle bound states of quarks or anti-quarks with the three different color charges, which are called *baryons*. The lightest color neutral state containing only quarks, the proton (uud), is stable. Extremely unstable bound states consisting of higher numbers of quarks can also exist, such as the pentaquark discovered in 2015 at the LHC. [44] Collectively, these multi-quark bound states are called *hadrons*.

Like leptons, the number of quarks in a state is conserved. However, because quarks cannot exist in an isolated state, that conservation described as a conservation of baryon number (B) defined similarly to lepton number. Mesons, because they have one quark and one antiquark, have $B = 0$.

2.1.2 *Forces*

The fermions in the previous section interact via the electromagnetic, weak, and strong forces. In a perturbative quantum field theory, interactions via these forces are represented by mediating bosons. These force carriers interact only with particles charged with their force's quantum numbers. The photon, for example, interacts only with electromagnetically charged particles. Gluons, mediators of the strong force, interact only with color charged particles, quarks and gluons. All fermions are weakly charged and interact with the weak force's mediators, the W and Z bosons.

The formulation for each of these forces is developed by requiring that the SM lagrangian be locally gauge invariant. [34] This can be accomplished by adding gauge fields to the lagrangian, whose behavior under gauge transformations cancels out the gauge dependence of the free lagrangian. However, adding a mass term for these fields reintroduces gauge dependence, so this mechanism only creates forces mediated by massless particles.

2.1.2.1 *The Electromagnetic Force*

The simplest example of gauge invariance requirements generating a description of a force can be found in electromagnetism. It has one massless mediator, the photon, which interacts with all electromagnetically charged particles. What follows is a brief description of how enforcing this invariance generates a lagrangian of the same form as the classical electromagnetic lagrangian, which can be easily incorporated into the SM.

The particles in Section 2.1.1 are fermions, and so their free lagrangians are Dirac lagrangians and all follow the form

$$\mathcal{L} = i\bar{\psi}\gamma^{\mu}\partial_{\mu}\psi - m\bar{\psi}\psi. \tag{1}$$

Requiring that the free lagrangians for these particles be invariant under a $U(1)$ local gauge transformation, $e^{iq\lambda(x)}$, can be accomplished by adding a term to the lagrangian which cancels the derivative term arising from λ's dependence on x:

$$\mathcal{L} = i\bar{\psi}\gamma^{\mu}\partial_{\mu}\psi - m\bar{\psi}\psi - (q\bar{\psi}\gamma^{\mu}\psi)A_{\mu} \tag{2}$$

where A_{μ} is a "gauge field" that transforms according to

$$A_{\mu} \rightarrow A_{\mu} + \partial_{\mu}\lambda. \tag{3}$$

This vector field must also come with a free term,

$$\mathcal{L} = -\frac{1}{16\pi}F^{\mu\nu}F_{\mu\nu} + \frac{1}{8\pi}m_A^2 A^{\nu}A_{\nu}. \tag{4}$$

The mass term for this field would not itself be invariant under the transformation, but the field can simply be made massless to avoid this problem. The final lagrangian, then, is

$$\mathcal{L} = i\bar{\psi}\gamma^{\mu}\partial_{\mu}\psi - m\bar{\psi}\psi - \frac{1}{16\pi}F^{\mu\nu}F_{\mu\nu} - (q\bar{\psi}\gamma^{\mu}\psi)A_{\mu} \tag{5}$$

which is precisely the original lagrangian with the addition of terms replicating the form of the Maxwell lagrangian. In a quantized interpretation, it describes a field that interacts with particles with non-zero electromagnetic charge q via interactions with a massless spin-1 boson, the photon.

For the purpose of succinct notation, this lagrangian is often rewritten in terms of the "covariant derivative"

$$\mathcal{D}_\mu = \partial_\mu + iq\lambda A_\mu \tag{6}$$

which immediately cancels the gauge dependent term created by the transformation. This mechanism is mathematically simple in the $U(1)$ case, but can be replicated for more complicated gauge transformations with perturbative approximations.

2.1.2.2 *Quantum Chromodynamics*

Quantum Chromodynamics (QCD), the theory describing the strong force, can be formulated similarly to the electromagnetic force, but with a $SU(3)$ transformation replacing $U(1)$. This transformation acts on a vector of equal mass quarks, the three different colors of a given flavor. The transformation is written as follows,

$$\boldsymbol{\psi} \to e^{-iq\boldsymbol{\lambda}\cdot\boldsymbol{\phi}(x)}\boldsymbol{\psi} \tag{7}$$

where $\boldsymbol{\phi}$ gives a vector of coefficients to be multiplied by the Gell-Man matrices, $\boldsymbol{\lambda}$. Though the math is more complicated than the $U(1)$ case in this higher dimensional rotation, the cancellation is ultimately similar.

The main difference, corresponding to this more complicated basis of transformations, is that eight fields A_μ are required rather than the one needed in electromagnetism. These eight fields correspond to eight massless bosons, the different color states of the gluon, the carrier of the strong force.

All together, the total lagrangian for QCD is

$$\mathcal{L} = i\bar{\psi}\gamma^\mu\partial_\mu\psi - m\bar{\psi}\psi - \frac{1}{16\pi}\boldsymbol{F}^{\mu\nu}\boldsymbol{F}_{\mu\nu} - (q\bar{\psi}\gamma^\mu\psi)\boldsymbol{A}_\mu, \tag{8}$$

an equation identical in form to Equation 5, with the mathematical complications of the additional fields hidden by the vector notation. In addition to that change, the covariant derivative must accommodate a vector $\boldsymbol{A}$ as well, changing only slightly to be defined as

$$\mathcal{D}_\mu = \partial_\mu + iq\boldsymbol{\lambda}\cdot\boldsymbol{A}_\mu. \tag{9}$$

This canceling is actually only satisfied to a first order expansion of the transformation, guaranteeing its validity only for infinitesimally small ϕ. However, the strong coupling constant, α, depends on the energy scale of the interaction, decreasing at higher energy scales and asymptotically increasing at low energies. Figure 2 shows this effect translated to distance scales, demonstrating that QCD is weak and can be considered perturbatively at small distance scales, but at large distance scales this approximation breaks down, and the colorless hadrons introduce in Section 2.1.1.2 must be used to describe interactions instead.

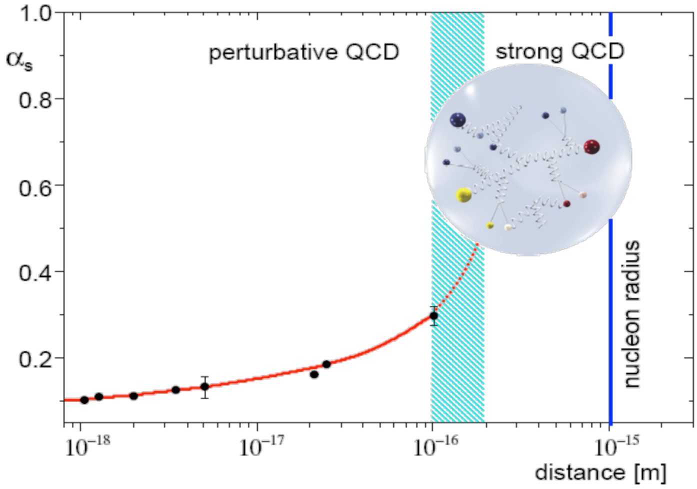

Figure 2: The running of the strong coupling constant, α. [42]

The boundary between these regimes is referred to as Λ_{QCD} and differentiates energies at which quarks can be considered free particles and the energies at which they must instead be described by their colorless bound states. The LHC is capable of producing individual quarks, but they instantaneously hadronize, producing showers of colored particles referred to as "jets".

2.1.2.3 *The Weak Force*

A similar process, using an $SU(2)$ gauge transformation, can produce a lagrangian that would suffice to describe the W and Z bosons of the SM, if only they were massless. However, they are not, so an alternate mechanism must be used to add masses to the lagrangian.

Before a mechanism for their masses was understood, and before they were discovered, the large mass of the W and Z bosons were proposed in order to unify the electromagnetic and weak forces into the electroweak force. The large masses were crucial to explain the discrepancy in the strength of the two forces.

This unified theory resulted in a triplet, $\boldsymbol{W}$, with coupling g_W, and a singlet field B, with coupling $g'/2$. However, this electroweak symmetry is broken, and mixing between these states occurs. Rewritten in their mass basis, the more familiar electroweak force carriers are produced: $W^{\pm}$, two states with identical coupling, Z^0, and A, the photon field.

2.1.2.4 *The Higgs Mechanism*

The reason for this symmetry breaking has to do with the final piece of the SM, the Higgs boson. The Higgs mechanism presents an alternate way to generate a mass term, through an unexpected route. It is a scalar field, with a lagrangian

$$\mathcal{L} = \frac{1}{2}(\partial_\mu \phi)^*(\partial^\mu \phi) + \frac{1}{2}\mu^2\phi^*\phi - \frac{1}{4}\lambda^4(\phi^*\phi)^2 \tag{10}$$

where ϕ is a complex scalar field, $\phi = \phi_1 + i\phi_2$. This looks very similar to the standard scalar field, but the signs on the mass and interaction terms are reversed, giving a result that looks like an imaginary mass. However, this lagrangian differs from all previously considered lagrangians in that its ground state does not occur at $\phi = 0$. Because this is a perturbative theory, its validity only holds when expanded around the ground states, which must satisfy

$$\phi_1^2 + \phi_2^2 = -\frac{\mu}{\lambda}. \tag{11}$$

Rewriting the original lagrangian in terms of fields centered around ground states chosen to satisfy that condition results in a reasonable mass term. However, in an effect called "spontaneous symmetry breaking", the original $SO(2)$ rotational symmetry of the lagrangian is lost, resulting only in a $U(1)$ rotational symmetry; the lagrangian is invariant under a phase transformation.

As in Section 2.1.2.1, it is possible to make the lagrangian invariant under a local $U(1)$ transformation, $\phi \rightarrow e^{i\theta(x)\phi}$ by adding a massless gauge field A^μ and using the covariant derivative. Due to the many cross terms from the non-zero ground state, terms for the mass of one of the bosons as well as the gauge field appear, leaving only one massless boson. The massless boson, it turns out, can be completely removed from the theory via local $U(1)$ transformations, ultimately producing a theory with one massive scalar (the Higgs) and a massive gauge field.

2.1.3 *Phenomenology of Proton-Proton Collisions*

As discussed in Chapter 3, the LHC collides bunches of high-energy protons, and the interactions of these protons' constituent quarks produce the wide array of particles seen in the ATLAS detector. The LHC typically cites its energy in terms of $\sqrt{S}$, the center of mass energy of protons in the two colliding beams. However, because the proton is not fundamental, this energy is divided among many particles that make up the proton.

To first order, a proton consists of three quarks: two up quarks and one down quark. However, a real quantum mechanical system is much more chaotic, with other quarks popping into and out of existence and gluons flying between them. These additional quarks are called "sea" quarks. The particles inside the proton can have a wide range of energies depending on the internal dynamics at the moment of the collision. These cannot be predicted exactly, but probabalistic models called PDFs describe the likelihood of any given configuration. These models are determined using data from hard scattering experiments and give probabalistic estimates for how often a given type of particle appears with a fraction x of the total proton energy, as seen in Figure 3.

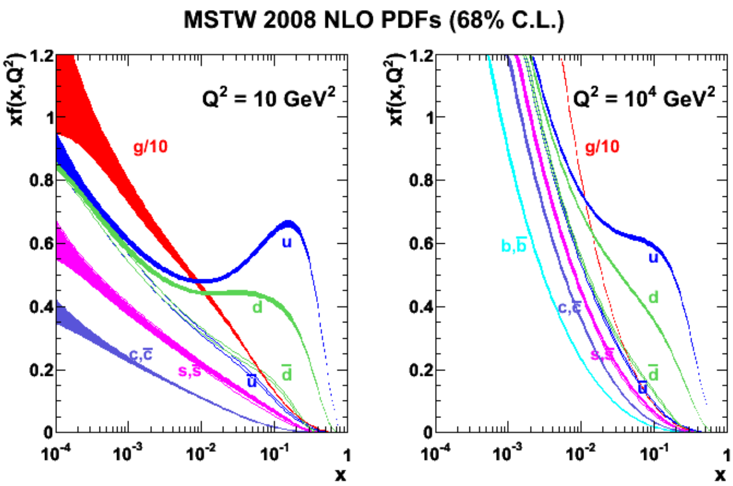

Figure 3: 2008 MSTW PDFs for various particle types. [41]

2.1.4 *Problems in the Standard Model*

Thought the SM is a self-consistent theory that describes to great accuracy all of the particles and forces in includes, it does have certain shortcomings. The most glaring is the omission of gravity. Though the force is well understood at large scales via the theory of General Relativity, no satisfying quantum description of gravity has been accepted, much less proven. The Planck scale, the energy scale at which gravitational interactions become large enough that no sound theory can ignore gravity, is at about $10^2 8$ eV, 16 orders of magnitude above the electroweak scale.

Another clear omission of the SM is Dark Matter (DM). This matter was first identified in 1933 through the observation of galactic rotation curves. [43] The speed of rotation indicated both that there was more mass in the system than could be accounted for by observations made directly of the galaxy, and that this additional matter was distributed in a halo, not a disk like the typical luminous matter. This effect can be seen in Figure 4. Since then, the gravitational impact of DM has been observed in colliding clusters and many more rotational curves, but it has never been directly detected or seen at a particle accelerator. As a consequence, very few details are known about the nature of the particles that make up this matter, only that it does not interact strongly or electromagnetically and its density throughout the universe.

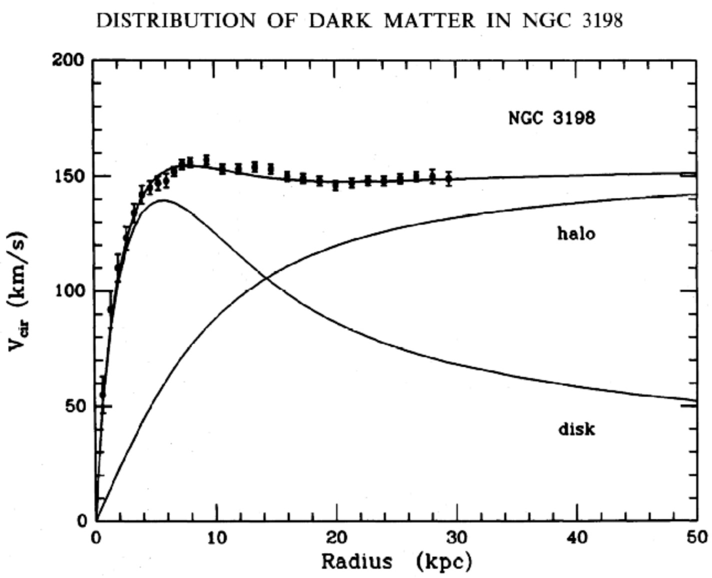

Figure 4: Galactic rotation curve showing that the discrepancy between the observed luminous matter and the total mass in the system can be described as a non-luminous halo of matter. [45]

Beyond the omissions of the SM, there are several aesthetic problems - things that could have no solution, but seem to suggest that the current SM are missing some pieces that could unify it and provide more order. The first is the sheer number of parameters in the SM. There are 26 independent parameters determining the mass of the particles and all the couplings between them. Besides the rough grouping of fermions into generations, there seems to be no order to masses of particles, and no way to predict the masses or couplings. Each, it seems, is independently provided by nature.

In the past, large numbers of seemingly unrelated parameters has indicated that a theory has a more fundamental form at shorter distance scales. The large number of elements, it turned out, could be explained by different groupings of three particles, the proton, neutron and electron. Later, the menagerie of hadrons became so large that a similar reimagining of what was fundamental took place, and the theory of quarks gave an order to the many mesons and baryons. This pattern leaves physicists suspicious or any theory with too many particles and free parameters, suggesting that perhaps, at a higher energy, there is a simpler model that can unify many of the seemingly disparate elements of the SM.

However, some of these seemingly independent parameters have suspicious symmetry. The Higgs mass, for example, has been measured to be 125 GeV. This mass is the sum of the bare mass, the one that appears in the lagrangian, and quantum corrections from interactions with other particles, which are proportional to the square of the particles' mass. Since new physics must exist at the Planck scale to account for gravity, these corrections could be up to 35 orders of magnitude larger than the Higgs mass. The bare mass could theoretically cancel out this massive correction, these parameters should be independent, and the odds that they would be precisely the same to 35 places are very, very small. This exact canceling is often called "fine-tuning", an undesirable trait in a theory which suggests that some more fundamental symmetry has been missed. The word "naturalness" is used to describe the the extent to which a theory is free of fine-tuning.

2.2 SUPERSYMMETRY

2.2.1 *Supersymmetry Phenomenology*

2.2.2 *Solutions to Standard Model Problems*

Many believe that a complete SM would include a unification of the three forces, as electromagnetism and the weak force have already been unified. This requires that at some higher energy, the coupling constants of all three forces merge.

2.2.3 *Supersymmetry Signatures in $p-p$ Collisions*

2.2.3.1 *Simplified Models Used in This Analysis*

2.3 MONTE CARLO GENERATORS

Part III

THE EXPERIMENT

This section describes the LHC and the ATLAS detector, which collectively provide the physical environment and the data collection for the analysis discussed in Part iv.

3 THE LARGE HADRON COLLIDER

The LHC is unique in the world, producing proton-proton collisions at energies an order of magnitude higher than any accelerator before. It provides unique environments at its collision points where massive, unstable particles can exist for an instant, then decay to the ordinary material of the universe. It is the goal of the ATLAS experiment to identify these short-lived particles, but LHC's work of producing them is equally complex.

3.1 OPERATION OF THE LARGE HADRON COLLIDER

4

THE ATLAS DETECTOR

The ATLAS detector circumscribes the LHC's beam pipe, enclosing the collision point with a series of particle detecting layers, aimed at making as many measurements of the particles leaving the collision point as possible. Its goal is to get a precise measurement of all the stable or semi-stable particles flying from proton-proton collisions at its center, allowing analyzers to fully reconstruct the kinematics of the underlying processes.

The ATLAS detector is the largest detector of its kind, measuring 44 m in length and 25 m in height, as seen in Figure 5. The size is mainly determined by the constraints of the MS, discussed in Section 4.4, which is the largest and outermost subsystem. The MS is submerged in a spatially varying magnetic field provided by three toroidal magnets, while the ID (Section 4.2) is encased by a superconducting solenoid, which provides a uniform 2 T field throughout its volume [2].

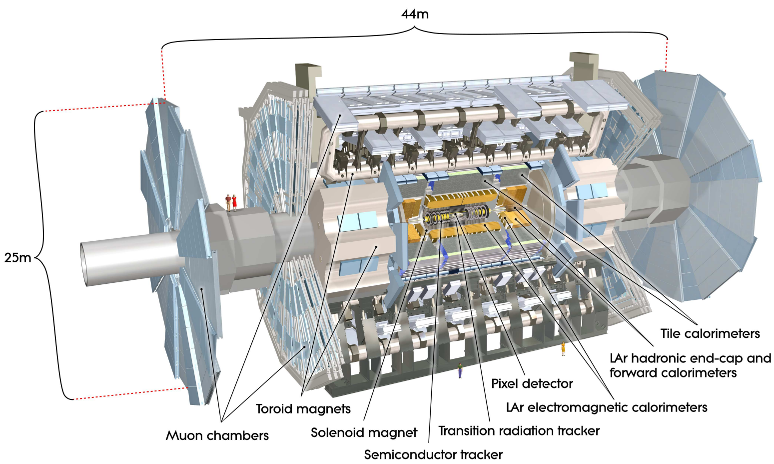

Figure 5: Diagram of the ATLAS detector, with subsystems and magnets identified.

4.1 COORDINATE SYSTEM USED IN THE ATLAS DETECTOR

The ATLAS detector is centered around a the collision point in the beam pipe, and is built radially out from the pipe, maintaining as much rotational symmetry as possible. It is also symmetric in the forward-backward directions. Because of this geometry, a coordinate system using the collision point as the origin is used, with the beam pipe defining the z-axis. The positive x direction is defined as pointing to the center of the LHC ring, while the positive y direction points upwards. For ease of reference, the side of the detector in the positive-z direction is referred to as the A side, and the other side is referred to as the C side.

Because of the radial design of the detector, angular coordinates are often used. The azimuthal angle ϕ defines the radial distance around the beam pipe and the polar angle θ defines the angle from the beam axis (z). However, a transformation of the polar angle called pseudorapidity (η) is used more often, and is defined as

$$\eta = -ln[tan\frac{\theta}{2}]. \tag{12}$$

Building on this variable definition, distance between objects is typically defined as

$$\Delta R = \sqrt{\Delta\eta^2 + \Delta\phi^2}. \tag{13}$$

Often variables are defined purely in the transverse plane, which is indicated by a subscripted T, as in p_T, which gives an object's transverse momentum. Another common usage is E_T^{miss}, which gives the negative vectorial sum of the energy in an event.

4.2 THE INNER DETECTOR

One goal of the ATLAS detector is to produce tracks, predictions of the paths particles take as they travel through the detector. Collisions in the detector produce about 1000 particles, so identifying and differentiating all these tracks is both a hardware and a computational challenge. The ID, also called the Tracker, is responsible for providing high enough resolution measurements that each of these tracks and its precise position can be recorded. This tracking system consists of three subdetectors which each produce electrical responses to charged particles passing through their active material. Each of these signals is called a hit. ATLAS tracking software considers all these hits and forms tracks, with the goal of minimizing fake tracks due to random noise. Some details of this process is discussed at length in Chapter 6. The full ID can be seen in Figure 6, while a schematic in Figure 7 demonstrates the η coverage of each detector.

4.2.1 *The Pixel Detector*

The Pixel detector lies closest to the beam pipe of the LHC, and has four layers comprising 92 million read-out channels. There are three

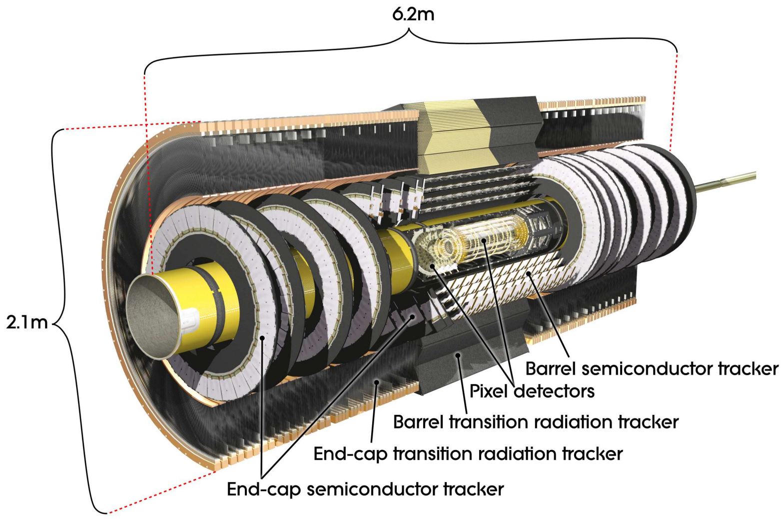

Figure 6: Diagram of the ATLAS Inner Detector, containing the Pixel, SCT, and TRT subsystems.

standard layers, referred to as Layers 1-3 (L1, L2, L3), and an additional layer added for the 2015 data-taking, called the Insertable B-Layer (IBL).

4.2.1.1 *The Original Pixel Detector*

The Pixel Detector consists of high-precision silicon chip pixel sensors, with 1744 sensors total. Each sensor is identical, containing 47232 pixels, which are typically each $50 \times 400\ \mu\text{m}^2$.

As shown in Figure 7, the central η region (barrel) is covered by three concentric cylindrical layers of sensors, while the higher η region (endcap) is covered by a series of three disks positioned in the $x - y$ plane. Together, they give complete coverage out to $\eta = 2.5$, and a particle coming from the collision point will typically by measured by three layers. Each of these measurements is accurate in the barrel (endcap) to 10 μm in the $R - \phi$ direction and 115 μm in the z (R) direction.

4.2.1.2 *Addition of the IBL*

In 2015, the IBL was lowered into the ATLAS cavern and added to the Pixel Detector. This layer sits on top of the beam pipe, inside barrel L1, which was formerly responsible for the first measurement of charged particles coming from a collision. TODO: add info about precision

As the IBL's' name suggests, it was added to improve detection of B mesons, whose non-trivial lifetimes create secondary vertices in ATLAS events, which allow them to be distinguished from other particles with precise track measurement. The IBL is closer to the interaction point and has a smaller resolution, giving it a better chance to see these slightly displaced vertices.

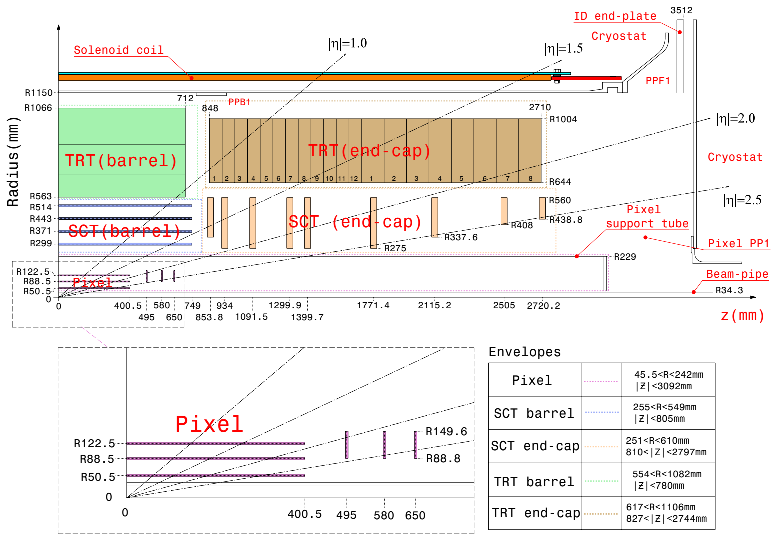

Figure 7: Diagram of one-quarter of the ATLAS Inner Detector, with lines drawn to indicate various η locations. The labels PP1, PPB1 and PPF1 indicate the patch-panels for the ID services. TODO: what is that.

4.2.2 *The Silicon Microstrip Tracker*

The Silicon Microstrip Tracker (SCT) employs similar technology to the Pixel Detector, with 15912 sensors and 6.3 million readout channels. Its difference from the Pixel Detector is in the readout, which is performed by a series of 12 cm long strips with a width of 80 μm. These layers are paired, placed on top of one another at a small (40 mrad) angle to allow for position determination in both directions, giving 4 spatial measurements for each particle passing through the SCT. In the barrel, these strips run parallel to the beam pipe, while in the endcap, they are arranged radially. These strips have a resolution in the barrel (endcap) of 17 μm in the $R - \phi$ direction and 580 μm in the z (R) direction.

4.2.3 *The Transition Radiation Tracker*

The Transition Radiation Tracker (TRT) uses 4mm diameter gas-filled tubes, each with a high voltage wire suspended along the center of the tube. The tubes run the length of the barrel, with a separate wire in the positive and negative z direction. In the endcap, the tubes are arranged radially. In total, there are about 351,000 readout channels in the TRT. This detector makes measurements only in the $R - \phi$ direction, where the resolution of each measurement is 130 μm. Each particle typically creates about 36 hits as it passes through the TRT.

TODO is any of this right? Particles passing through the gas mixture of the TRT ionize the gas, producing electrons which drift towards the wire due to a potential difference applied between it and the straw. This process takes about 48 ns, and the signal can be directly read out, giving the fastest measurement of particles in the ID. This speedy readout is essential to triggering, discussed more in Section 4.6.

The TRT also responds to low-energy transition radiation photons, which produce a much larger signal than charged particles passing through the detector. Because of this strong difference in signals, hits from the TRT are used to help differentiate between electrons and photons in the detector.

4.3 THE CALORIMETERS

Unlike the tracking detectors, which aim to take measurements of a particle with minimal alterations of its trajectory, the calorimeters measure the the energy of objects by stopping them entirely. The calorimeters, which can be seen in Figure 8, provide coverage out to $\eta < 4.9$. Higher granularity electromagnetic measurements are made within $|\eta| < 2.5$, where the ID provides tracking capability, in order to give precision measurements of the energy of photons and electrons, and provide reduced resolution measurements at higher η. The hadronic calorimeters provides coarser granularity, which is sufficient to determine the energy of jets.

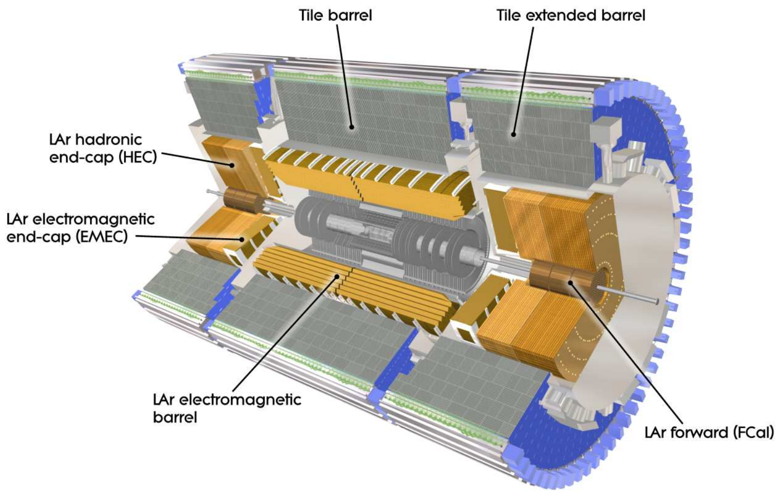

Figure 8: The calorimeter system of the ATLAS detector.

Another task of the calorimeter system is to limit punch-through to the MS, described in Section 4.4. All other particles must be fully stopped by the calorimeters to allow for clean signals from muons, and to measure the total energy of the particle. This requirement sets minimum sizes for each of the calorimeters.

THE LAR ELECTROMAGNETIC CALORIMETER uses liquid argon as its active detector medium alternating with layers of lead acting as the absorber. The layers are shaped like accordions, which allows for complete coverage with multiple layers of active material, three in central η ($0 < |\eta| < 2.5$) and two at higher η ($2.5 < |\eta| < 3.2$). At $|\eta| < 1.8$, an instrumented liquid argon presampler provides a measurement of energy lost prior to reaching the calorimeters.

THE TILE CALORIMETER is a hadronic calorimeter which surrounds the LAr Calorimeter. It uses layers of steel as its absorber with scintillating tiles as the active material between them, which are read out by photomultiplier tubes. The Tile Calorimeter covers $|\eta| < 1.7$.

THE LAR HADRONIC ENDCAP CALORIMETER covers the hadronic calorimetery for higher η. It uses liquid argon active material and copper plate absorbers. This calorimeter covers $1.5 < |\eta| < 3.2$, overlapping with the hadronic calorimeters in either direction of its η range.

THE FCAL or forward calorimeter provides electromagnetic and hadronic coverage at very high η ($3.1 < |\eta| < 4.9$). This calorimeter also uses liquid argon as its active material, and uses copper-tungsten as the absorber.

4.4 THE MUON SPECTROMETER

The MS measures charged particles that escape from the calorimeter system. Because the calorimeters are designed to completely absorb the energy of electrons, photons, hadrons, and jets, the MS mainly detects muons, which escape from the calorimeter with very little loss of energy. The goal of the MS is to give a high-precision measurement of these muons, and also to be able to quickly identify events with muons for the sake of triggering, discussed in Section 4.6. The layout of the MS can be seen in Figure 9 and Figure 10. Muons can be measured for all $|\eta|$<2.7, and they can be triggered on for $|\eta|$<2.4. The entire system is about 24m tall and 40m long.

To achieve these goals, the MS has several subsystems. The system responsible for precision measurement is called the Monitored Drift Tubes (MDTs). This subdetector consists of chambers of three to eight layers of tubes, with three layers of chambers covering both the barrel and end-cap regions. The tubes each contain an Ar/CO_2 gas mixture and a single high voltage wire which runs at its center along its length. Charged particles excite the gas as they pass through it, producing electrons which drift towards the high voltage wire. The resulting electric signal is read out, and the magnitude and timing of the signals are both used to differentiate particle traces from noise.

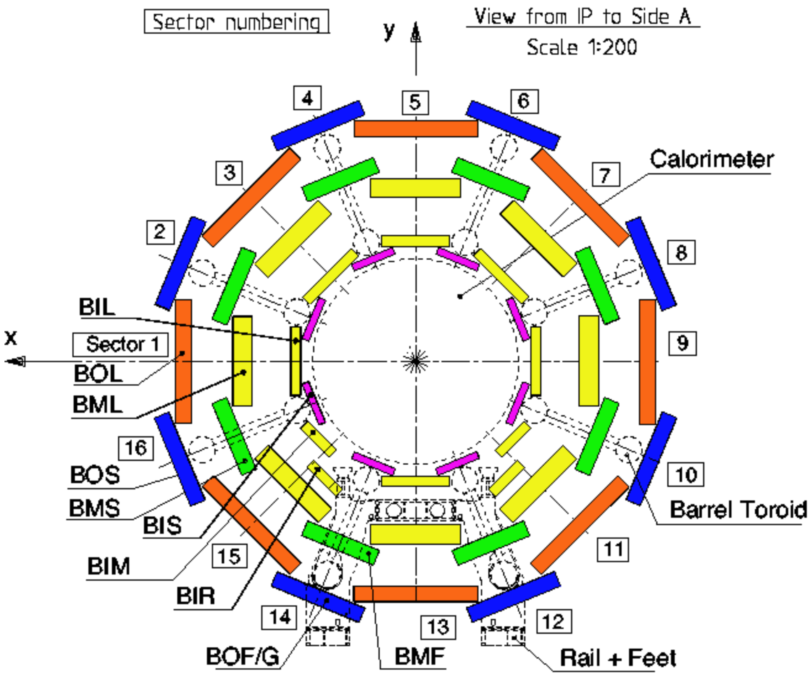

Figure 9: An x-y view of the MS. In it, the three barrel layers are visible, as well as the overlapping, differently sized chambers. The outer layer of the MS is about 20m in diameter.

Though very effective at giving a precise measurement, the MDTs have several shortcomings. The first is that the measurement is only precise in the direction perpendicular to the tubes; in the direction parallel to them, the resolution is not much better than the length of the drift tube. The resolution in the perpendicular direction is about 35 μm with the combined measurement of all the tubes in a chamber.

The MDTs are slow, with a maximum drift time of about 700ns. Because collisions occur every 25ns, this readout cannot be used for triggering. In addition, in high-rate regions of the detector, the MDTs are very susceptible to having multiple hits in one readout window. To minimize this effect, another detector called the Cathode-Strip Chambers (CSCs) is used. This detector consists of multi-wire proportional chambers which have cathode strips on either side of the anode in orthogonal directions, allowing for a 40μm resolution in one direction and 5mm resolution in the other. Their drift times are also much faster than the MDTs, at about 40ns, so they are placed in the forward region of the detector ($2<|\eta|<2.7$) where the incident particle rates are much higher.

To achieve rates fast enough to be used for triggering, the Resistive Plate Chambers (RPCs) and Thin Gap Chambers (TGCs) are used. These chambers can produce track information roughly as fast as the collision rate. The RPCs are used in the barrel and are made up of two high-resistance plastic plates with a gas mixture under an electric field between them. Passing particles ionize this gas, and the result-

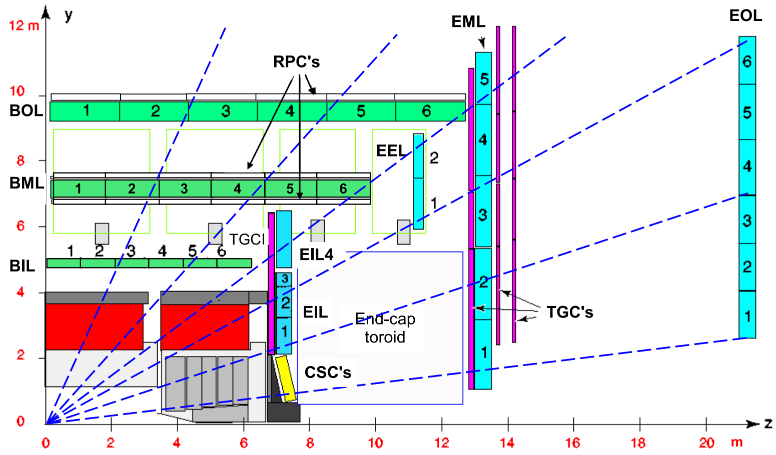

Figure 10: An r-z view of the MS. The three layers of the barrel and end-cap MS are visible, and all muons at $|\eta|<2.7$ should traverse three detectors, assuming they propagate in an approximately straight line from the interaction point.

ing signal is read out via metallic strips mounted to the plastic plates. The TGCs used in the endcap are a form of multi-wire proportional chambers, like the CSCs. Unlike the CSCs, the cathode is placed extremely close to the wires, speeding up its operation.

The massive system is also subject to deformations due to gravity. To maintain this good precision, these deformations are constantly monitored in each chamber with a set of four optical alignment rays, which give alignment information at the precision of $<30\mu$m. In addition, a sag-adjustment system can use this information to re-align any wires that droop under gravity's pull. Lastly, the MS can be aligned using the tracks made from hits it measures, discussed more in Section 5.3.

4.5 THE MAGNET SYSTEM

The ATLAS magnet system consists of four superconducting magnets: an inner solenoid, a barrel toroid, and two endcap toroids. Collectively, they are 22m in diameter and 26m long, and their basic layout can be seen in Figure 11.

The solenoid sits inside the calorimeter volume and provides a uniform 2T magnetic field to particles traveling through the ID. This axial field causes the trajectories of charged particles to bend in the $x-y$ plane, and measurements of the curvature of these trajectories give the most accurate p_{T} measurement for many particles.

Because the solenoid sits between the tracking system and the calorimeter, it is important that it interfere minimally with particles in order to allow the calorimeter to measure their full energies.

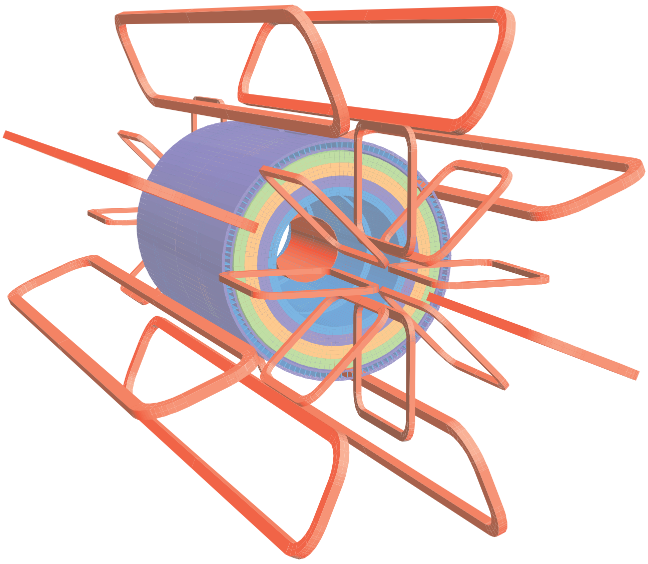

Figure 11: The magnet system of the ATLAS detector. The inner cylinder shows the solenoid which gives a uniform magnetic field in the ID. Outside of that are the barrel and endcap toroids, which provide a non-uniform magnetic field for the MS.

4.6 THE TRIGGER SYSTEM

5 OBJECT RECONSTRUCTION IN THE ATLAS DETECTOR

5.1 electrons

5.2 photons

5.3 muons

5.4 jets

5.5 missing transverse energy

5.6 monte carlo simulation

6 APPLICATION OF A NEURAL NETWORK TO PIXEL CLUSTERING

6.1 CLUSTERING IN THE PIXEL DETECTOR

Creating tracks from individual hits in the Inner Detector is one of most computationally challenging parts of the reconstruction of ATLAS events. Each event typically contains thousands of hits in the pixel detector alone, which must be combined into one coherent picture of which particles traversed the detector, and how they moved and lost energy as they traveled. A typical particle deposits charge in several pixels per layer, forming a series of clusters which can be connected together to form a track. This track can in turn be used to measure the charge, momentum, and trajectory of the particle, and in many cases, provides ATLAS's most precise measurement of a charged particle.

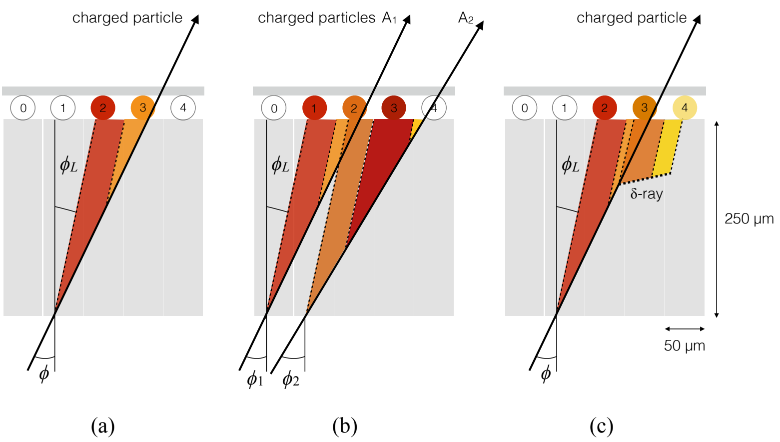

Figure 12: A few possible types of clusters in the Pixel Detector. (a) shows a single particle passing through a layer of the detector, (b) shows two particles passing through the detector, creating a single merged cluster, and (b) shows a single particle emitting a δ-ray as it passes through the detector.

The process of going from clusters to track is relatively simple in an isolated environment in which one particle travels cleanly through all the layers, but can be complicated by multiple close-by tracks and by a single particle's emission of low energy particles, called δ-rays. In these cases, it can be hard to tell how many particles were involved in creating a cluster, and where exactly each of those particles passed through the layer. A few examples of these cases can be seen in Figure 12 . The process of determining which pixels with charge deposits belong to a single particle is called clustering, and it has recently been updated from a charge interpolation method to a method using a NN.

6.1.1 *Charge Interpolation Method*

A typical cluster contains a few pixel hits spanning in the x and y directions, each with its own measurement of charge deposition, or Time Over Threshold (ToT). The extent of the cluster is defined by grouping together any pixels with a shared edge or corner. In the charge interpolation method, also called the CCA clustering algorithm, these individual hits are combined to make one estimation of the position a single particle which passed through them, using the following equation:

$$x_{cluster} = x_{center} + \Delta_x(\phi, N_{row}) \cdot \left[\Omega_x - \frac{1}{2}\right] \tag{14}$$

$$x_{cluster} = x_{center} + \Delta_x(\phi, N_{row}) \cdot \left[\Omega_x - \frac{1}{2}\right] \tag{15}$$

where $\Omega_{x(y)}$ is defined by

$$\Omega_{x(y)} = \frac{q_{last\ row(col)}}{q_{first\ row(col)} + q_{last\ row(col)}} \tag{16}$$

and q represents the ToT of a given pixel, and $\Delta_{x(y)}$ is a function derived from either data or MC and produces an output related to the projected length of the particles track on the pixel sensor and is measured as a function of ϕ, the incident angle of a particle on the sensor, and $N_{row(col)}$, the number of pixels in the x and y direction.

In a simple case, such as (a) of Figure 12 , this method works quite effectively. However, in cases like (b), it has no ability distinguish two-particle from one-particle clusters, and can only assign a cluster center between the two particles' locations, despite that intermediate pixel having the lowest ToT. Furthermore, because this method can't differentiate two-particle clusters, the tracking software can't use that information to preferentially allow multiple tracks to be fit to the cluster. In cases like (c), the δ-ray will bias the measurement of the particle's position in whichever direction it is emitted.

6.1.2 *Improving Measurement with Neural Networks*

To address these problems, a series of NNs were created [6]. The first determines the number of particles in a given cluster, the second predicts their positions within the cluster, and the third assesses the uncertainty of the position measurement.

These NNs are all trained with:

- a 7×7 grid of cluster ToT information[1]
- a 7-element vector containing the y-size of the pixels in the grid
- the layer of the pixel detector that the cluster was observed in
- a variable indicating whether the cluster is located in the barrel or endcap
- θ and ϕ variables projecting the incident angles of the particle on the sensor, assuming it comes from the interaction point
- the η index of the pixel module

After the Number NN predicts a number of particles associated with the cluster, required to be between 1 and 3, the same inputs are fed to one of three Position NNs based on the determined number of particles, which then outputs the x and y positions of each of the particles. Then, the same inputs combined with the output of the Position NN are fed into one of three Error NNs (also distinguished by number of particles), which outputs an uncertainty for each of the position predictions made. An example of the output of this process can be seen in Figure 13, where the improved position resolution from the ability to identify a multi-particle cluster is evident. The particle location predictions from the NNs are then handed to the tracking software, which is able to independently consider multiple locations from a given cluster to find the best fit.

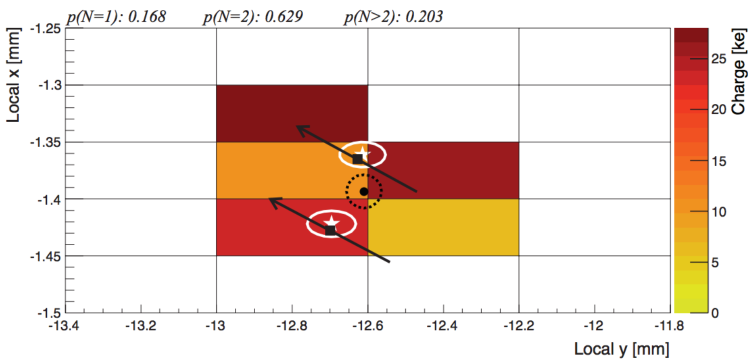

Figure 13: One example of a two-particle cluster and its truth information compared with the output of the NNs. At top, the $p(N = i)$ values give the output of the Number NN, the probabilities that the cluster contains 1, 2, and 3 particles. Given the highest probability is for $N = 2$, the other NNs predict the postion and errors of the two particles (in white). The black arrows and squares represent the truth information from the cluster, and the black dot and dotted line show the position measurement for the un-split cluster.

1 Clusters spanning more than seven pixels in either direction are split into multiple clusters.

6.2 IMPACT OF THE NEURAL NETWORK

The NN was first applied to 7 TeVdata, where it improved position resolution for particles in small and large clusters. Figure 14 shows the improvement from the addition of the NN in x resolution in different cluster sizes. The improvement from CCA clustering is particularly evident in the 4-pixel case, where the double peaked structure of the interpolation method has been completely removed with the NN.

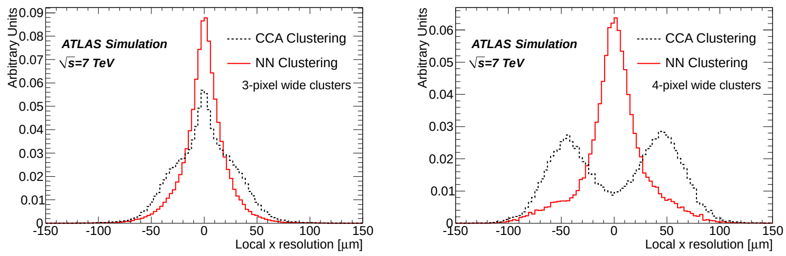

Figure 14: x resolutions for clusters with 3 (left) and 4 (right) pixels in the x direction in 7 TeVdata for CCA and NN clustering.

6.2.1 *The Neural Network in 13 TeV Data*

In Run 2, the tracking algorithm is first run on the CCA clusters, where it constructs loose tracks that allow shared clusters, clusters to which multiple tracks are fit [9]. The NN is then used to identify which clusters are likely to have had multiple particles pass through them, and to identify the positions of those particles. In the case that the cluster is determined to have resulted only from one particle, tracks that share that cluster are penalized.

With this configuration, studies were done to determine how accurately MC could model the NN's response to data. Figure 15 shows a comparison of how often the NN identifies different types of clusters in data and MC. Very good agreement was seen between the two samples.

With this confirmation that studies performed in MC would be good indicators for performance on data, the robustness of the NN was investigated with 13 TeVMC [10]. The goal of these studies was to determine which variables the NN's predictions were most sensitive to, and whether it was likely that these variables could be mismodeled enough to produce unexpected results. One example of a sensitive variable is the overall charge scale, and the impact of its scaling can be seen in Figure 16. In this case, the likelihood to misidentify multi-particle clusters and single particle clusters depended significantly on this scaling. Overall, it was found that variations on the cluster charge produced a significant impact on predictions, while all other variations had a minimal effect.

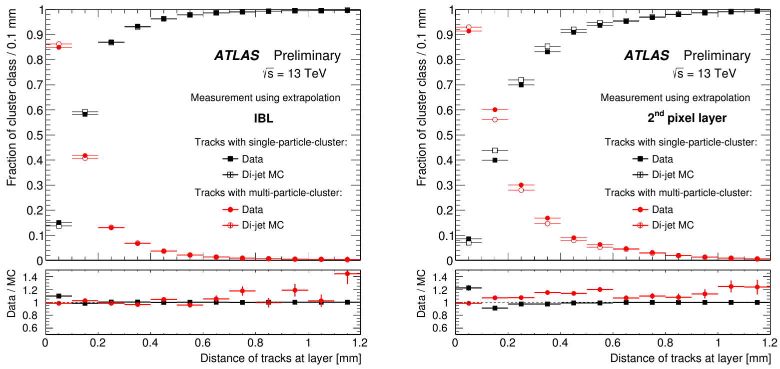

Figure 15: Fraction of cluster classes as a function of the distance between tracks for (a) IBL and (b) 2nd pixel layer.

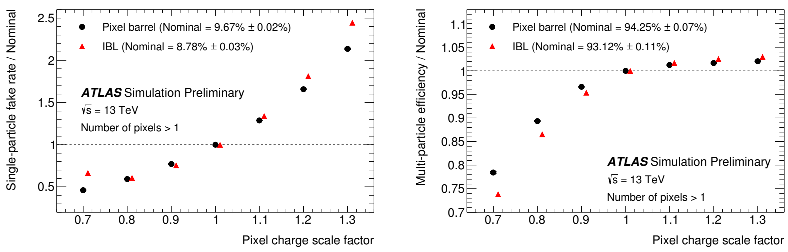

Figure 16: Performance of the pixel neural network used to identify clusters created by multiple charged particles, as a function of constant coherent scaling of the charge in each pixel in the cluster. The left figure shows the rate at which the neural network wrongly identifies clusters with one generated particle as clusters with multiple particles. The right figure shows the rate at which the neural network correctly identifies clusters generated by multiple particles as such.

Part IV

SEARCHING FOR SUPERSYMMETRY

This section describes an analysis of the ATLAS data carried out by the author and her analysis team. The analysis was performed on events from $p-p$ collisions provided by the LHC at $\sqrt{s}$=13 TeV. It searches for events like those described in Section 2.2.3.1, which contain a Z boson decaying to leptons, jets, and missing transverse energy. The selection of a signal region in which to search for these events, background estimates, systematic uncertainty estimates, results, and interpretations are all discussed.

7 BACKGROUND PROCESSES

This analysis is fundamentally a search for Supersymmetry in events with two leptons whose invariant mass is consistent with a Z boson. Additional event selections are made to reduce Standard Model processes relative to potential Supersymmetric processes, defined by simplified models discussed in Section 2.2.3.1. Supersymmetric events typically have large amounts of $E_{\mathrm{T}}^{\mathrm{miss}}$, H_{T} (the scalar sum of the p_{T} of objects in the event), and many jets. All of these features can help isolate these events from backgrounds. To understand what cuts would optimize the sensitivity of the search, it is essential to first understand what these Standard Model backgrounds are.

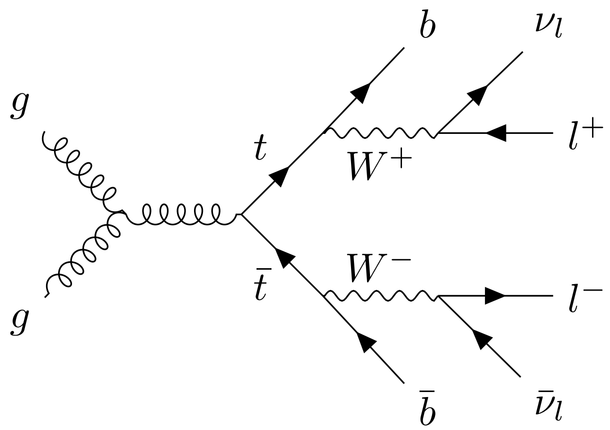

Figure 17: An example Feynman diagram of $t\bar{t}$ production and decay.

$t\bar{t}$ is the largest background for this search. Figure 17 shows an example of this process, which can decay to many jets, leptons, and neutrinos, which are seen in the detector as $E_{\mathrm{T}}^{\mathrm{miss}}$. Thus, $t\bar{t}$ naturally has high $E_{\mathrm{T}}^{\mathrm{miss}}$ and H_{T}, jets, and leptons from two different W boson decays, which may coincidentally form an invariant mass on the Z peak. These events are very difficult to separate from potential signals, though keeping the mass window small and increasing $E_{\mathrm{T}}^{\mathrm{miss}}$ and H_{T} above the typical values for $t\bar{t}$ events can help reduce them.

DIBOSON production is the next leading background. These events can contain real Z bosons and will peak on-Z like a signal. In addition, in events like Figure 18, an additional W boson can decay to another lepton and a neutrino, providing $E_{\mathrm{T}}^{\mathrm{miss}}$. The pictured process can occur with associated jets, but at reduced rates, so adding a jet requirement to the signal region can help reduce these events. If the

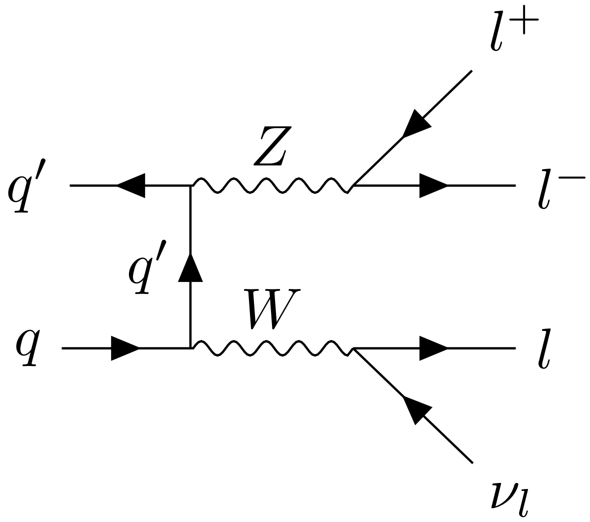

Figure 18: An example Feynman diagram of the production and decay of a WZ event.

W boson in this diagram instead decayed to two jets, there would be no true $E_{\mathrm{T}}^{\mathrm{miss}}$ from a neutrino, so a $E_{\mathrm{T}}^{\mathrm{miss}}$ cut in conjunction with a jet cut is very effective in reducing the total diboson background.

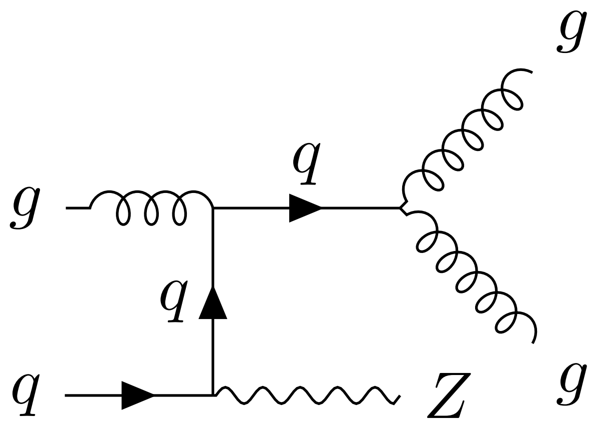

Figure 19: An example Feynman diagram of the production and decay of a $Z/\gamma^* +$ jets event.

$Z/\gamma^* +$ JETS processes are very common but, as shown in Figure 19, don't produce any true $E_{\mathrm{T}}^{\mathrm{miss}}$ or a very large number of jets. Thus a high H_{T} cut can help reduce this background, but a $E_{\mathrm{T}}^{\mathrm{miss}}$ cut is the most powerful. Events with very mismeasured jets or leptons can fake high $E_{\mathrm{T}}^{\mathrm{miss}}$, but these drastic mismeasurements are rare.

Other processes can contribute to the Standard Model background at lower rates. Processes similar to $Z/\gamma^* +$ jets but with a W boson instead of a Z have real $E_{\mathrm{T}}^{\mathrm{miss}}$ from leptonic W decays, but only one lepton. However, a fake or non-prompt lepton can cause these events to look very similar to simulated signals. Additionally, there are rare processes such as $t\bar{t}$ in association with bosons that will also be difficult to separate from signal processes.

7.1 MONTE CARLO SAMPLES

To precisely compare simulated signal to backgrounds, MC samples are generated for each of these processes. Table 1 details the method used to produce each sample. With these and the simulated background, optimizations on a signal regioin can be made to maximize potential for discovery or exclusion of simplified Supersymmetric models. These comparisons and the signal region definition can be found in Section 9.1.

Physics process	Generator	Parton Shower	Cross section	Tune	PDF set
$t\bar{t}+W$ and $t\bar{t}+Z$ [14, 33]	MG5_aMC@NLO	Pythia 8.186	NLO [26, 40]	A14	NNPDF23LO
$t\bar{t}+WW$ [14]	MG5_aMC@NLO	Pythia 8.186	LO [18]	A14	NNPDF23LO
$t\bar{t}$ [17]	Powheg Box v2 r3026	Pythia 6.428	NNLO+NNLL [30, 31]	Perugia2012	NLO CT10
Single-top (Wt) [17]	Powheg Box v2 r2856	Pythia 6.428	Approx. NNLO [36]	Perugia2012	NLO CT10
WW, WZ and ZZ [16]	Sherpa 2.1.1	Sherpa 2.1.1	NNLO [25, 27]	Sherpa default	NLO CT10
$Z/\gamma^*(\rightarrow \ell\ell)$ + jets [15]	Sherpa 2.1.1	Sherpa 2.1.1	NNLO [28, 29]	Sherpa default	NLO CT10

Table 1: Simulated background event samples used in this analysis with the corresponding matrix element and parton shower generators, cross-section order in α_s used to normalise the event yield, underlying-event tune and PDF set.

8 OBJECT IDENTIFICATION AND SELECTION

8.1 ELECTRONS

Cut	Value/description
Baseline Electron	
Acceptance	$p_{\mathrm{T}} > 10$ GeV, $\lvert\eta^{\mathrm{clust}}\rvert < 2.47$
Quality	`LHLoose`
Signal Electron	
Acceptance	$p_{\mathrm{T}} > 25$ GeV, $\lvert\eta^{\mathrm{clust}}\rvert < 2.47$
Quality	`LHMedium`
Isolation	`GradientLoose`
Impact parameter	$\lvert z_0 \sin\theta\rvert < 0.5$ mm
	$\lvert d_0/\sigma_{d_0}\rvert < 5$

Table 2: Summary of the electron selection criteria. The signal selection requirements are applied on top of the baseline selection.

8.2 MUONS

8.3 JETS

8.4 PHOTONS

Cut	Value/description
Baseline Muon	
Acceptance	$p_{\mathrm{T}} > 10$ GeV, $\|\eta\| < 2.5$
Quality	`Medium`
Signal Muon	
Acceptance	$p_{\mathrm{T}} > 25$ GeV, $\|\eta\| < 2.5$
Quality	`Medium`
Isolation	`GradientLoose`
Impact parameter	$\|z_0 \sin\theta\| < 0.5$ mm
	$\|d_0/\sigma_{d_0}\| < 3$
isBadMuon	MCP isBadMuon Flag

Table 3: Summary of the muon selection criteria. The signal selection requirements are applied on top of the baseline selection.

9

EVENT SELECTION

Table 4: Overview of all signal, control and validation regions used in the on-shell Z search. More details are given in the text. The flavour combination of the dilepton pair is denoted as either "SF" for same-flavour or "DF" for different flavour. All regions require at least two leptons, unless otherwise indicated. In the case of CRγ, VR-WZ, VR-ZZ, and VR-3L the number of leptons, rather than a specific flavour configuration, is indicated. The main requirements that distinguish the control and validation regions from the signal region are indicated in bold. Most of the kinematic quantities used to define these regions are discussed in the text. The quantity $m_{\mathrm{T}}(\ell_3, E_{\mathrm{T}}^{\mathrm{miss}})$ indicates the transverse mass formed by the $E_{\mathrm{T}}^{\mathrm{miss}}$ and the lepton which is not assigned to either of the Z-decay leptons.

On-shell Z **regions**	$E_{\mathrm{T}}^{\mathrm{miss}}$ **[GeV]**	$H_{\mathrm{T}}^{\mathrm{incl}}$ **[GeV]**	n_{jets}	$m_{\ell\ell}$ **[GeV]**	**SF/DF**	$\Delta\phi(\mathbf{jet}_{12}, \boldsymbol{p}_{\mathrm{T}}^{\mathrm{miss}})$	$m_{\mathrm{T}}(\ell_3, E_{\mathrm{T}}^{\mathrm{miss}})$ [GeV]	$n_{\text{b-jets}}$
Signal region								
SRZ	> 225	> 600	≥ 2	$81 < m_{\ell\ell} < 101$	SF	> 0.4	–	–
Control regions								
CRZ	$<$ **60**	> 600	≥ 2	$81 < m_{\ell\ell} < 101$	SF	> 0.4	–	–
CR-FS	> 225	> 600	≥ 2	$\mathbf{61 < m_{\ell\ell} < 121}$	**DF**	> 0.4	–	–
CRT	> 225	> 600	≥ 2	$\mathbf{> 40, m_{\ell\ell} \notin [81, 101]}$	SF	> 0.4	–	–
CRγ	–	> 600	≥ 2	–	$0\ell, 1\gamma$	–	–	–
Validation regions								
VRZ	$<$ **225**	> 600	≥ 2	$81 < m_{\ell\ell} < 101$	SF	> 0.4	–	–
VRT	**100–200**	> 600	≥ 2	$\mathbf{> 40, m_{\ell\ell} \notin [81, 101]}$	SF	> 0.4	–	–
VRS	**100–200**	> 600	≥ 2	$81 < m_{\ell\ell} < 101$	SF	> 0.4	–	–
VR-FS	**100–200**	> 600	≥ 2	$\mathbf{61 < m_{\ell\ell} < 121}$	**DF**	> 0.4	–	–
VR-WZ	**100–200**	–	–	–	$\mathbf{3\ell}$	–	< 100	0
VR-ZZ	< 100	–	–	–	$\mathbf{4\ell}$	–	–	0
VR-3L	**60–100**	$>$ **200**	≥ 2	$81 < m_{\ell\ell} < 101$	$\mathbf{3\ell}$	> 0.4	–	–

9.1 SIGNAL REGION

9.2 CONTROL AND VALIDATION REGIONS

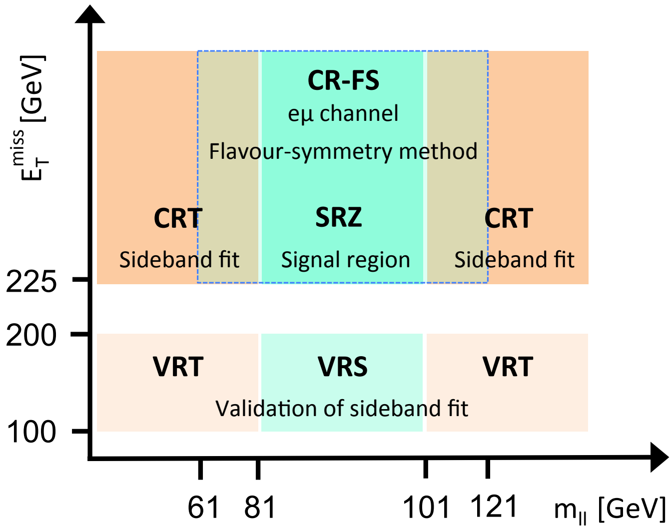

Figure 20: Schematic diagrams of the control, validation and signal regions for the on-shell Z (top) and edge (bottom) searches. For the on-shell Z search the various regions are shown in the $m_{\ell\ell} - E_{\mathrm{T}}^{\mathrm{miss}}$ plane, whereas in the case of the edge search the signal and validation regions are depicted in the $H_{\mathrm{T}} - E_{\mathrm{T}}^{\mathrm{miss}}$ plane.

Trigger	L1	Notes
Single electron triggers		
HLT_e60_lhmedium	L1_EM22VHI	2015 and 2016
HLT_e60_lhmedium_nod0	L1_EM22VHI	2016 Only
HLT_e26_lhtight_nod0_ivarloose	L1_EM22VHI	Isolated; for evaluation in 2016
Di-electron triggers		
HLT_2e12_lhloose	L1_2EM13VH	2015 Only
HLT_2e17_lhvloose_nod0	L1_EM15VH	2016 Only
Single muon triggers		
HLT_mu50	L1_MU20	2015 and 2016
Di-muon triggers		
HLT_mu18_mu8noL1	L1_MU15	2015 Only
HLT_2mu14_nomucomb	L1_MU10	2016 Only
Electron-muon triggers		
HLT_e17_lhloose_mu14	L1_EM15VH_MU10	2015 Only
HLT_e7_lhmedium_mu24	L1_MU20	2015 Only
HLT_e17_lhloose_nod0_mu14	L1_MU10_EM15VH	2016 Only
HLT_e7_lhmedium_nod0_mu24	L1_MU20	2016 Only

Table 5: List of the triggers considered for this analysis. The corresponding L1 items are included for reference. The last column notes if the trigger is available in data.

Lepton p_T	Trigger in 2015	Trigger in 2016
Di-electron channel		
$p_T(e_1) > 65$ GeV	HLT_e60_lhmedium	HLT_e60_lhmedium_nod0
$p_T(e_1) \leq 65$ GeV	HLT_2e17_lhloose	HLT_2e17_lhvloose_nod0
Di-muon channel		
$p_T(\mu_1) > 52.5$ GeV	HLT_mu50	HLT_mu50
$p_T(\mu_1) \leq 52.5$ GeV	HLT_mu24_mu8noL1	HLT_2mu14_nomucomb
Electron-muon channel		
$p_T(e) > 65$ GeV	HLT_e60_lhmedium	HLT_e60_lhmedium_nod0
$p_T(e) \leq 65$ GeV and $p_T(\mu) > 52.5$ GeV	HLT_mu50	HLT_mu50
$p_T(e) \leq 65$ GeV and $p_T(\mu) \leq 52.5$ GeV and $p_T(e) < p_T(\mu)$	HLT_e7_lhmedium_mu24	HLT_e7_lhmedium_nod0_mu24
$p_T(e) \leq 65$ GeV and $p_T(\mu) \leq 52.5$ GeV and $p_T(\mu) < p_T(e)$	HLT_e17_lhloose_mu14	HLT_e17_lhloose_nod0_mu14

Table 6: Lepton trigger requirements used for the analysis in different regions of lepton-p_T phase space.

10 BACKGROUND ESTIMATION

This analysis requires two leptons that reconstruct to a Z mass, jets, $E_{\mathrm{T}}^{\mathrm{miss}}$, and H_{T}. Any standard model processes that produce this signature will appear as a background to the search. The most important task of the analysis is to identify and estimate these backgrounds, so that any excess of events appearing on top of the standard model background can be identified. The main backgrounds for this analysis are described in Chapter 7. The largest background is from flavor symmetric processes, with smaller contributions coming from diboson processes, $Z/\gamma^* + \text{jets}$, rare top processes, and fake and non-prompt leptons.

10.1 FLAVOR SYMMETRIC PROCESSES

FS backgrounds include any processes that produce pairs of leptons with uncorrelated flavor in the final state. In this analysis, the largest contribution comes from $t\bar{t}$, with additional events from processes like WW and $Z \to \tau\tau$. In these processes, each lepton comes from a different decay. Unlike a $Z \to \ll$ decay then, these leptons' flavors are completely independent.

10.1.1 *Flavor Symmetry Method*

As a consequence of the independence of the lepton flavors, any FS process should produce ee, $\mu\mu$, and $e\mu$ events in a 1:1:2 ratio. This ratio is taken advantage of by the flavor symmetry method by measuring $e\mu$ events in data and using them to predict the contribution of these processes in the ee and $\mu\mu$ channels. [12]

To estimate the number of events in SRZ, a control region called CR-FS is used. Both regions are defined in Table 4. CR-FS is very similar to SRZ with two changes: it requires different-flavor leptons instead of the same-flavor leptons required by SRZ, and the $m_{\ell\ell}$range it covers has been expanded by a factor of three, now ranging from 61 to 121 GeV. The expansion of the $m_{\ell\ell}$window is done to increase the number of events in the control region, thus lowering the statistical uncertainty of the prediction[1].

1 Though this statistical uncertainty is no longer dominant for the analysis, the method was developed for a smaller dataset for which this expansion dramatically decreased the total uncertainty on the background prediction. [4] Because of previous excesses seen, the signal region was not reoptimized for the larger dataset used in this search,

This control region is expected to be about 95% pure in FS processes, with most of the remaining events coming from fake or non-prompt leptons. The FS portion is made up primarily of $t\bar{t}$ (∼80%), with additional contributions from Wt (∼10%), WW (∼10%), and $< 1\%$ $Z \to \tau\tau$.

After the number of data events are measured in CR-FS, correction factors are applied to account for trigger efficiencies, selection efficiencies, the $m_{\ell\ell}$expansion, and the purity of the control region. Combining these factors, the estimate for number of events in the ee and $\mu\mu$ channels is as follows:

$$N_{ee}^{\text{est}} = \frac{1}{2} \cdot f_{\text{FS}} \cdot f_{Z\text{-mass}} \cdot \sum^{N_{e\mu}^{\text{data}}} k_e(p_{\text{T}}^{\mu}, \eta^{\mu}) \cdot \alpha(p_{\text{T}}^{\ell_1}, \eta^{\ell_1}), \tag{17}$$

$$N_{\mu\mu}^{\text{est}} = \frac{1}{2} \cdot f_{\text{FS}} \cdot f_{Z\text{-mass}} \cdot \sum^{N_{e\mu}^{\text{data}}} k_\mu(p_{\text{T}}^{e}, \eta^{e}) \cdot \alpha(p_{\text{T}}^{\ell_1}, \eta^{\ell_1}), \tag{18}$$

where $N_{e\mu}^{\text{data}}$ is the number of data events observed in CR-FS, f_{FS} is the FS purity in CR-FS, $f_{Z\text{-mass}}$ is the fraction of events in the widened $m_{\ell\ell}$range expected to be in the on-Z range (taken from $t\bar{t}$ MC), $k_e(p_{\text{T}}, \eta)$ and $k_\mu(p_{\text{T}}, \eta)$ are relative selection efficiencies for electrons and muons, calculated in bins of p_{T} and η of the lepton to be replaced, and $\alpha(p_{\text{T}}, \eta)$ accounts for the different trigger efficiencies for events in each channel, binned based on the kinematics of the leading lepton. These k and α factors are calculated from data in an inclusive on-Z selection ($81 < m_{\ell\ell}/$ GeV < 101, ≥ 2 jets), according to:

$$k_e(p_{\text{T}}, \eta) = \sqrt{\frac{N_{ee}^{\text{meas}}}{N_{\mu\mu}^{\text{meas}}}} \tag{19}$$

$$k_\mu(p_{\text{T}}, \eta) = \sqrt{\frac{N_{\mu\mu}^{\text{meas}}}{N_{ee}^{\text{meas}}}} \tag{20}$$

$$\alpha(p_{\text{T}}, \eta) = \frac{\sqrt{\epsilon_{ee}^{\text{trig}}(p_{\text{T}}, \eta) \times \epsilon_{\mu\mu}^{\text{trig}}(p_{\text{T}}, \eta)}}{\epsilon_{e\mu}^{\text{trig}}(p_{\text{T}}, \eta)} \tag{21}$$

where $\epsilon_{ee/\mu\mu}^{\text{trig}}$ is the trigger efficiency [2] and $N_{ee/\mu\mu}^{\text{meas}}$ is the number of $ee/\mu\mu$ events in the inclusive on-Z region described above. Here $k_e(p_{\text{T}}, \eta)$

---

but in future iterations of this analysis, the signal region have tighter cuts, making this decreased statistical uncertainty significant once again.

2 This efficiency is defined by taking all events in the inclusive on-Z selection mentioned above and determining the fraction that passes the relevant trigger requirement defined by Table 6. Because the offline selection made on these events already has some trigger dependence, this calculation of efficiency could be slightly biased. This effect is considered in Section 11.1.1, and the uncertainty applied to the estimate as a result is described.

Region	ee prediction	$\mu\mu$ prediction	combined prediction
	Prediction for 14.7 fb^{-1} of 2015+2016 Data		
SRZ	16.50 ± 2.11	16.67 ± 2.04	33.16 ± 3.94
VRS	49.70 ± 4.61	49.60 ± 4.56	99.31 ± 8.47

Table 7: Yields in signal and validation regions for the flavor symmetric background. Errors include statistical uncertainty, uncertainty from MC closure, uncertainty from the k and α factors, uncertainty due to deriving triggers efficiencies from a DAOD, and uncertainty on the MC shape used to correct for the $m_{\ell\ell}$expansion.

$= 1/k_{\mu}(p_{\mathrm{T}}, \eta)$, and this k factor is calculated separately for leading and sub-leading leptons, and the appropriate k value is selected based on the position of the lepton to be replaced.

Electron, muon, and trigger efficiencies are all quite close to one, and as a consequence, these correction factors are typically within 10% of unity, except in the region $|\eta| < 0.1$ where, because of the lack of coverage of the muon spectrometer, they are up to 50% from unity.

The estimate is corrected for contamination of non-FS backgrounds in CR-FS. A scaling factor is determined by subtracting these backgrounds from the number of $e\mu$ events measured in CR-FS, then determining the fraction of the original data events that this pure-FS number represents. The estimate for the other backgrounds is taken from MC for all processes except fakes, which are predicted from data using the matrix method described in Section 10.3.

A prediction is made both for the signal region, SRZ, and the lower-$E_{\mathrm{T}}^{\mathrm{miss}}$ validation region, VRS. This process is performed separately for the two data taking periods, 2015 and 2016, because of the changing triggers and conditions. The results are then summed together, as shown in Table 7. The uncertainties in this table are discussed in Section 11.1.1.

10.1.2 *Sideband Fit Method*

As a crosscheck to the flavor symmetry method, a MC-based method is used. This method is called a “sideband fit,” and it begins with a MC estimate of the signal region across a $m_{\ell\ell}$range that includes all values above 40 GeV. This region, excluding the on-Z range that makes up the Signal Region (SR), is used as a control region, defined as CRT in Table 4.

The total data yield is measured in CRT, and the MC is fit to match this yield with one normalization factor which scales the overall $t\bar{t}$ background. As mentioned in the previous section, $t\bar{t}$ is the dominant FS background, making up about 80% of the total events. All other backgrounds contributing to this control region are constrained by their uncertainties, which are used as nuisance parameters in the fit. The normalization factor from this fit is then applied to the $t\bar{t}$ MC yield in the SR, and combined with the MC predictions of the other FS processes in the SR to give a final estimate of this background. The results of the fit can be seen in Table 8.

The method is repeated in VRS to validate the method. The normalization factors, listed in Table 9, are significantly different for the two regions. This is expected because there is a known problem in which the $t\bar{t}$ MC over-predicts the high-$E_{\mathrm{T}}^{\mathrm{miss}}$ tail. This effect can be seen in a data-MC comparison in Figure 21. This is likely due to a mismodeling of of the top quark p_{T} distribution, which does not match the spectrum seen in data [13, 24]. However, this method corrects for this mismodeling by performing fits in regions very kinematically similar to the signal region.

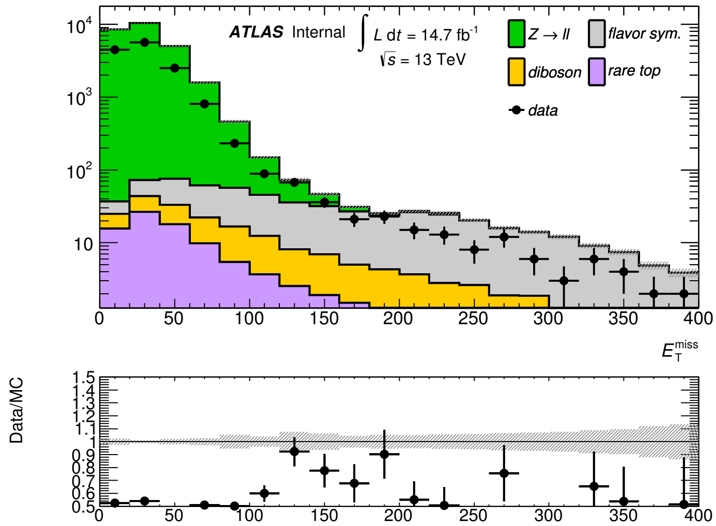

Figure 21: Comparison of data and MC in a selection like SRZ, without the $E_{\mathrm{T}}^{\mathrm{miss}}$ cut.

This method is extremely effective as a crosscheck because it uses a completely independent dataset from the flavor symmetry method, and the two methods have very little overlap in dependence on MC. They produce consistent results in both SRZ and VRS, as shown in Table 10.

10.2 $Z/\gamma^* +$ JETS BACKGROUND

The Z/γ^* + jets background is mainly produced by a process called Drell-Yan in which annihilating quark/anti-quark pairs produce a Z boson or a virtual photon. These bosons then decay to two leptons, which, in the case of the Z boson, naturally appear in the Z-mass window. The boson typically recoils off a hadronic system, which

channel	$ee/\mu\mu$ CRT	$ee/\mu\mu$ SRZ	ee SRZ	$ee/\mu\mu$ SRZ
Observed events	273	60	35	25
Fitted bkg events	272.76 ± 16.88	49.33 ± 8.04	27.09 ± 4.73	22.70 ± 3.80
Fitted flavour symmetry events	236.96 ± 21.66	28.96 ± 7.47	16.41 ± 4.33	12.55 ± 3.29
Fitted WZ/ZZ events	4.03 ± 1.13	14.27 ± 4.45	7.81 ± 2.45	6.46 ± 2.07
Fitted Sherpa $Z/\gamma^* +$ jets events	1.95 ± 0.14	0.00 ± 0.00	0.00 ± 0.00	0.00 ± 0.00
Data-driven $Z/\gamma^* +$ jets ($\gamma +$ jets) events	0.00 ± 0.00	3.10 ± 2.25	$1.02^{+1.25}_{-1.02}$	2.08 ± 1.38
Fitted rare top events	4.04 ± 1.04	2.90 ± 0.76	1.39 ± 0.38	1.50 ± 0.40
Data-driven fake lepton events	25.78 ± 14.26	$0.10^{+0.18}_{-0.10}$	0.46 ± 0.45	0.10 ± 0.01
MC exp. SM events	366.71	61.01	33.73	27.74
MC exp. flavour symmetry events	331.32	40.72	23.09	17.63
MC exp. WZ/ZZ events	4.02	14.20	7.77	6.43
MC exp. Sherpa $Z/\gamma^* +$ jets events	1.94	0.00	0.00	0.00
Data-driven exp. $Z/\gamma^* +$ jets ($\gamma +$ jets) events	0.00	3.10	1.02	2.08
MC exp. rare top events	4.04	2.89	1.39	1.50
Data-driven exp. fake lepton events	25.39	0.10	0.46	0.10

Table 8: Background fit results from the sideband fit method. The $t\bar{t}$ MC's normalization is taken as a free parameter in the fit to data in CRT, then that normalization factor is applied in SRZ. The results are shown here both divided between the ee and $\mu\mu$ channels and summed together. All other backgrounds are taken from MC in CRT, while in SRZ, the $Z/\gamma^* +$ jets contribution is taken from the $\gamma +$ jets method. The uncertainties quoted include both statistical and systematic components.

Fit region	$t\bar{t}$ normalization
CRT	0.64 ± 0.18
VRT	0.80 ± 0.09

Table 9: Summary of the $t\bar{t}$ normalization factors calculated by the sideband fit to CRT and VRT for the 2015+2016 data.

Region	Flavour-symmetry	Sideband fit
SRZ	33 ± 4	29 ± 7
VR-S	99 ± 8	92 ± 25

Table 10: Comparison of FS background predictions from the nominal method, the flavor symmetry method, and the cross-check, the sideband fit method. Uncertainties include statistical and systematic uncertainties in both cases.

can produce the jet and H_{T} requirement required in SRZ. However, this process rarely produces real $E_{\mathrm{T}}^{\mathrm{miss}}$ (though occasionally neutrinos do appear in its hadronic decays), so events often appear with high $E_{\mathrm{T}}^{\mathrm{miss}}$ values due to extreme mismeasurement. Because SRZ cuts on the very high $E_{\mathrm{T}}^{\mathrm{miss}}$ tails of a Z distribution, a small change in the assumptions about jet resolution or energy scale in MC can drastically change the prediction, and a low $Z/\gamma^* +$jets prediction can result in a signal-like peak appearing in the final result.

Because of this inaccuracy in the MC prediction in these high $E_{\mathrm{T}}^{\mathrm{miss}}$ tails, a data-driven method is used to estimate this background. The method takes γ+jets events which, like the $Z/\gamma^* +$jets events, contain one boson recoiling against a hadronic system, and corrects for the kinematic differences between γ and Zs [3, 23]. These sample of photons used in taken from CR-γ, which is similar to the SRZ selection without the $E_{\mathrm{T}}^{\mathrm{miss}}$ requirement, but it vetoes leptons and requires at least one photon. Additionally, the $\Delta\phi(\mathrm{jet}_{12}, \boldsymbol{p}_{\mathrm{T}}^{\mathrm{miss}})$ cut, which is designed to reduce the background from mismeasured jets, is removed for this region because of its unpredictability at very low values of $E_{\mathrm{T}}^{\mathrm{miss}}$, when the angle of the $E_{\mathrm{T}}^{\mathrm{miss}}$ is much less meaningful.

The most significant experimental difference between Z and photon events is that Z bosons rapidly decay, in the case of this analysis, to two leptons, which can then be observed by the ATLAS detector. In contrast, the photon is stable, and can be directly detected by ATLAS. This means that the reconstructed Z boson and the directly observed photon have very different energy resolutions.

10.3 FAKES

The fakes background consists of processes that produce only one lepton, but whose events are otherwise kinematically similar to the SR. These processes include semileptonic $t\bar{t}$, W+jets processes, and single top. Though these processes typically only produce one lepton, they can be reconstructed with two leptons due to a hadron being misidentified as a lepton or from real non-prompt lepton resulting from photon conversions or b-hadron decays. As such, it includes both events that have been properly reconstructed and many that are included in the SR due to imperfect reconstruction. As with the $Z/\gamma^* +$jets background, it is very difficult to predict with MC because the flaws in reconstruction are typically less well described by the models used in MC production than the successes. Nonetheless, a rough estimate can be made of this background by using MC, which indicates that the number of fake events in SRZ is consistent with zero.

Despite the small predicted contribution in the SR, a data-driven method called the "matrix method" is employed to estimate these fake events [11]. This method is also used to estimate the fakes contribution to other control and validation regions where their effect is often more significant.

In the matrix method, the quality requirements for signal leptons are loosened to give a selection of baseline leptons (see Table 2 and Table 3), which consist of a higher fraction of fake leptons. In each CR, VR, or SR, the remaining kinematic selections are made on the baseline leptons, and the number of leptons in that region which pass the signal lepton requirements (N_{pass}) and the number which fail (N_{fail}) are measured. For a 1-lepton selection, these quantities can be used to predict the number of fake events that pass the selection according to:

$$N^{\text{fake}}_{\text{pass}} = \frac{N_{\text{fail}} - (1/\epsilon^{\text{real}} - 1) \times N_{\text{pass}}}{1/\epsilon^{\text{fake}} - 1/\epsilon^{\text{real}}}. \tag{22}$$

The efficiencies ϵ^{real} and ϵ^{fake} give the relative identification efficiency from baseline to signal for genuine, prompt leptons and fake and non-prompt leptons, respectively. For a 2-lepton selection, the principle is the same, but the equation is more complicated, and it requires four-by-four matrix to account for possible combinations of real and fake leptons.

To calculate ϵ^{real}, the tag-and-probe method is performed a selection of $Z \to \ell\ell$ data events, CR-real, described in Table 11. In this method, one "tag" lepton passing a signal selection is required, as is another "probe" lepton passing a baseline requirement. Distributions of $m_{\ell\ell}$for tag + passing probe and tag + failing probe are then fit, and the efficiency is computed using the ratio acquired from the fit. A comparison of data and MC in CR-real can be seen in Figure 22.

Fakes regions	$E_{\mathrm{T}}^{\mathrm{miss}}$ **[GeV]**	H_{T} **[GeV]**	$n_{\mathbf{jets}}$	$m_{\ell\ell}$ **[GeV]**	**SF/DF**	**OS/SS**	n_{ℓ}
CR-real	–	$> \mathbf{200}$	≥ 2	**81–101**	2ℓ SF	OS	2
CR-fake	$< \mathbf{125}$	–	–	> 12	2ℓ **SF/DF**	**SS**	≥ 2

Table 11: Control regions used to measure efficiencies of real and fake leptons. The flavour combination of the dilepton pair is denoted as either "SF" for same-flavour or "DF" for different flavour. The charge combination of the leading lepton pairs are given as "SS" for same-sign or "OS" for opposite-sign.

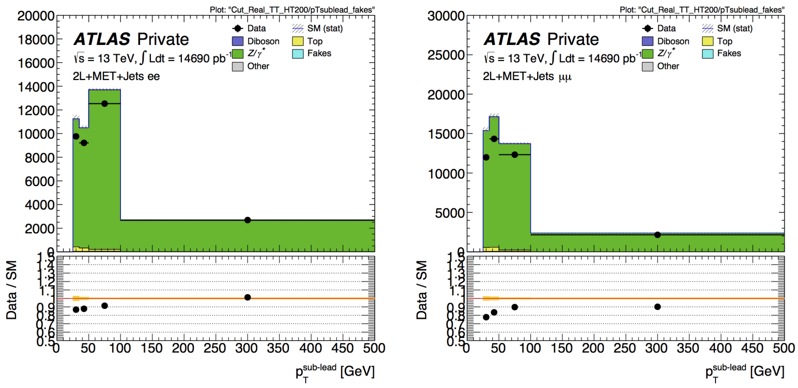

Figure 22: Sub-leading lepton p_{T} for ee (left) and $\mu\mu$ (right) events in the tight-tight region used to measure the real-lepton efficiency for 2016.

The fake efficiency, ϵ^{fake}, is determined using the tag-and-probe method in CR-fake, also described in Table 11. This region is different from all other regions considered in this analysis because it requires same-sign leptons. Very few processes genuinely produce two same-sign leptons, so this region is enhanced in fake leptons. An upper limit on $E_{\mathrm{T}}^{\mathrm{miss}}$ is placed on CR-fake to limit the possible contamination from BSM processes. According to MC, real, prompt leptons make up about 7% (11%) of the baseline electron (muon) sample and about 10% (61%) of the signal electron (muon) sample. These backgrounds are subtracted from the CR-fake yields when calculating the efficiencies. Figure 23 shows a comparison of data and MC in this region.

This method is validated in a fakes-rich validation region with a same-sign lepton requirement, $E_{\mathrm{T}}^{\mathrm{miss}}$ ≥50GeV, ≥2 jets, and a veto on $m_{\ell\ell}$on the Z-mass peak for same flavor channels. The results of this validation can be seen in Figure 24. With the systematic uncertainties

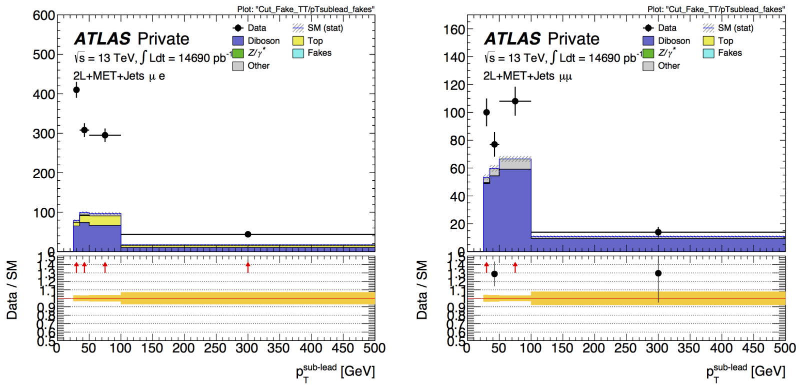

Figure 23: Sub-leading lepton p_T for μe (left) and $\mu\mu$ (right) events in the tight-tight region used to measure the fake-lepton efficiency for 2016.

included, the prediction agrees well with the data across a wide range of $m_{\ell\ell}$values.

10.4 DIBOSON AND RARE TOP PROCESSES

The remaining backgrounds are diboson processes (excluding WW, which is included in the FS background) and rare top processes. Dibosons events make up about 30% of the events in SRZ, while rare top process contributions are much smaller. Both are taken directly from MC, with validation regions to confirm the accuracy of the prediction. These regions are Table 4, and target different parts of these backgrounds. VR-ZZ is a four-lepton selection designed to select a very pure sample of ZZ events. VR-WZ requires three leptons and specific cuts on m_T, the transverse mass, and E_T^{miss} in order to select mostly $WZ \to lllv$ events. VR-3L is similar to VR-S, but loosens the H_T and E_T^{miss} cuts and requires at least three leptons. This region is designed to target any $\geq$ 3-lepton process in a region as kinematically close to SRZ as possible while still maintaining enough events to validate. The makeups of these multilepton validation regions, as well as VRS, are shown in Table 12.

To confirm that the kinematics are well modeled in the diboson validation regions, distributions of boson mass and p_T are shown in MC and data. Figure 25 shows these distributions for VR-WZ, and Figure 26 shows these distributions for VR-ZZ.

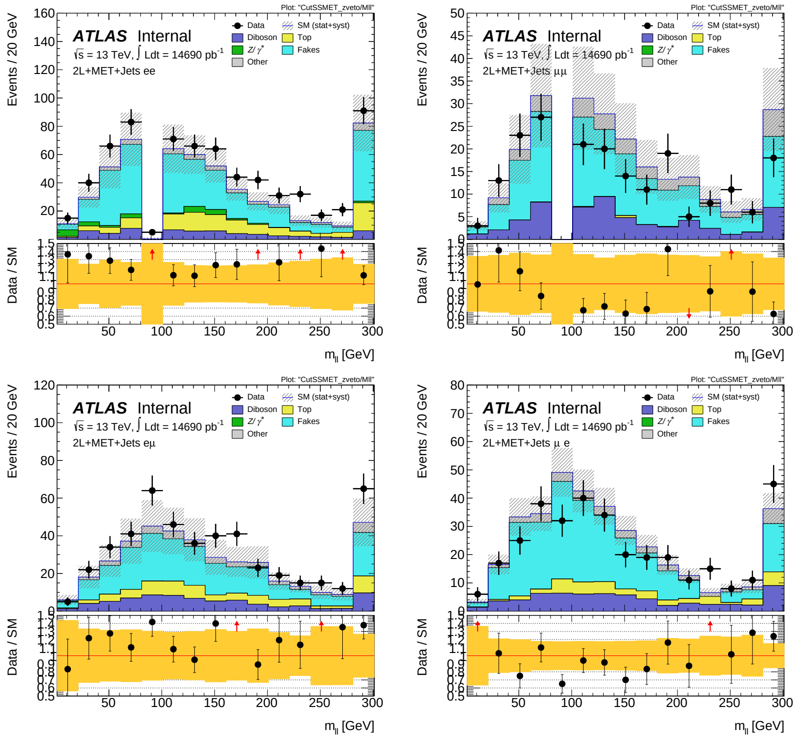

Figure 24: Same sign validation regions in the ee (top left), $\mu\mu$ (top right), $e\mu$ (bottom left) and μe (bottom right) channels combining 2015+2016 data. Uncertainty bands include both statistical and systematic uncertainties.

	VR-S	VR-WZ	VR-ZZ	VR-3L
Observed events	236	698	132	32
Total expected background	224 ± 41	613 ± 66	139 ± 25	35 ± 10
Flavour-symmetric	99 ± 8	-	-	-
WZ/ZZ events	27 ± 13	573 ± 66	139 ± 25	25 ± 10
Rare top events	11 ± 3	14 ± 3	0.44 ± 0.11	9.1 ± 2.3
$Z/\gamma^* +$jets events	84 ± 37	-	-	-
Fake lepton events	4 ± 4	26 ± 6	-	0.6 ± 0.3

Table 12: Yields in validation regions. In VRS, data-driven background estimates are used for $Z/\gamma^* +$jets, fakes, and FS processes. All other backgrounds are taken from MC, including all backgrounds in the multi-lepton VRs. Uncertainties include statistical and systematic components.

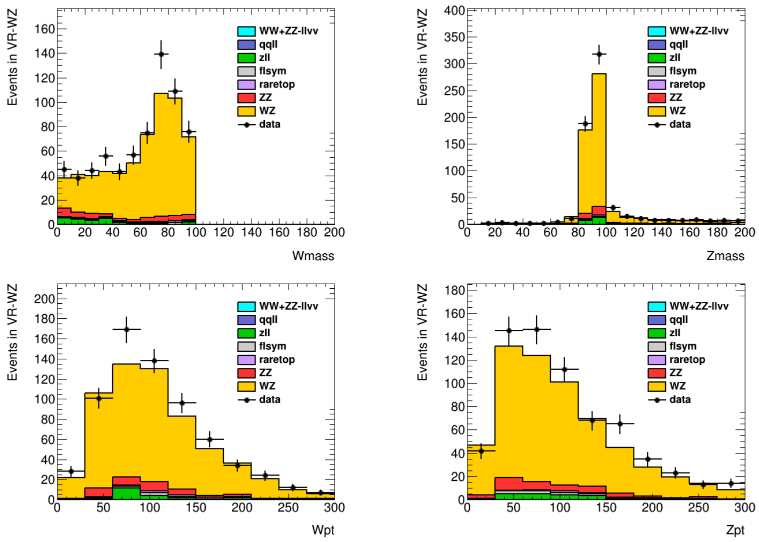

Figure 25: Distribtuions in VR-WZ. On the top row, reconstructed transverse mass of the W (left) and mass of the Z (right). On the bottom row, p_T of the W (left) and Z (right).

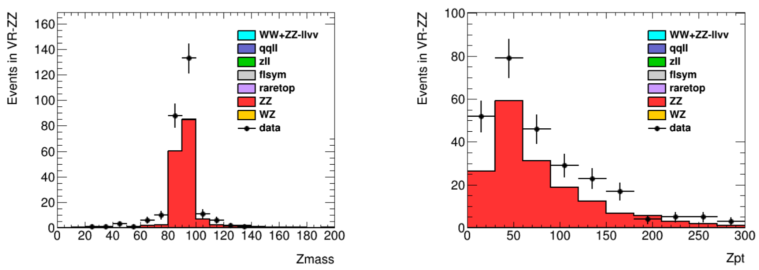

Figure 26: Distribtuions in VR-WZ. On the left, mass of the Z bosons in the event, and on the right, p_T of the Z bosons.

11 SYSTEMATIC UNCERTAINTIES

11.1 UNCERTAINTIES ON DATA-DRIVEN BACKGROUNDS

11.1.1 *Uncertainties on the Flavor Symmetry Method*

The flavor symmetry method is a data driven method that makes its primarily on based events populating an SR-like Control Region (CR) in the different-flavor channel. The statistical uncertainty on these events makes up the dominant uncertainty on the method. To reduce this uncertainty, the $m_{\ell\ell}$range on the CR is expanded, tripling the number of events in CR-FS. Though this reduces the statistical uncertainty significantly, it is still significantly higher than any of the other systematic uncertainties on this method, as seen in Table 13. Also included in the statistical uncertainty column is the uncertainty on the number of non-FS events in CR-FS, which is used to scale the prediction to remove any contamination in the CR.

Reg.	Ch.	Pred.	Uncertainties					
			stat.	MC clos.	k and α	dAOD usage	$m_{\ell\ell}$ shape	total
SRZ	ee	16.50	1.82	0.88	0.53	0.12	0.22	2.11
	$\mu\mu$	16.67	1.83	0.79	0.33	0.11	0.23	2.04
	ee+$\mu\mu$	33.16	3.66	1.07	0.86	0.23	0.45	3.94
VRS	ee	49.70	3.21	2.34	2.20	0.34	0.75	4.61
	$\mu\mu$	49.60	3.14	2.88	1.40	0.31	0.75	4.56
	ee+$\mu\mu$	99.31	6.34	4.00	3.60	0.65	1.49	8.47

Table 13: Uncertainties in the on-Z signal and validation regions. Nominal predictions are given with statistical uncertainty (including uncertainty from subtracted backgrounds), MC Closure uncertainty, uncertainty on the prediction from varying k and α by their statistical uncertainties, comparing the efficiencies from AODs to that of DAODs, and on the $m_{\ell\ell}$widening, which includes MC statistics and a data/MC comparison in a loosened region.

The next largest contribution to the uncertainty comes from MC closure tests, which are used to determine how effective the method is in its prediction. If, for example, using weights derived from an inclusive selection at high $E_{\mathrm{T}}^{\mathrm{miss}}$ lead to a bias, the closure test would indicate that and an appropriate uncertainty could be placed on the estimate based on the difference between the MC and the prediction. In this test, the entire FS procedure is performed on $t\bar{t}$ MC, including a recalculation of weighting factors α and k. The prediction from $e\mu$ events in MC is compared to the MC ee and $\mu\mu$ events, as seen in Figure 27. The difference between the two predictions is then summed in quadrature with the statistical uncertainty on each prediction to give the total closure uncertainty seen in Table 13. In these closure tests, all predictions agree within the statistical uncertainty, so the bulk of the resulting error is due to MC statistics.

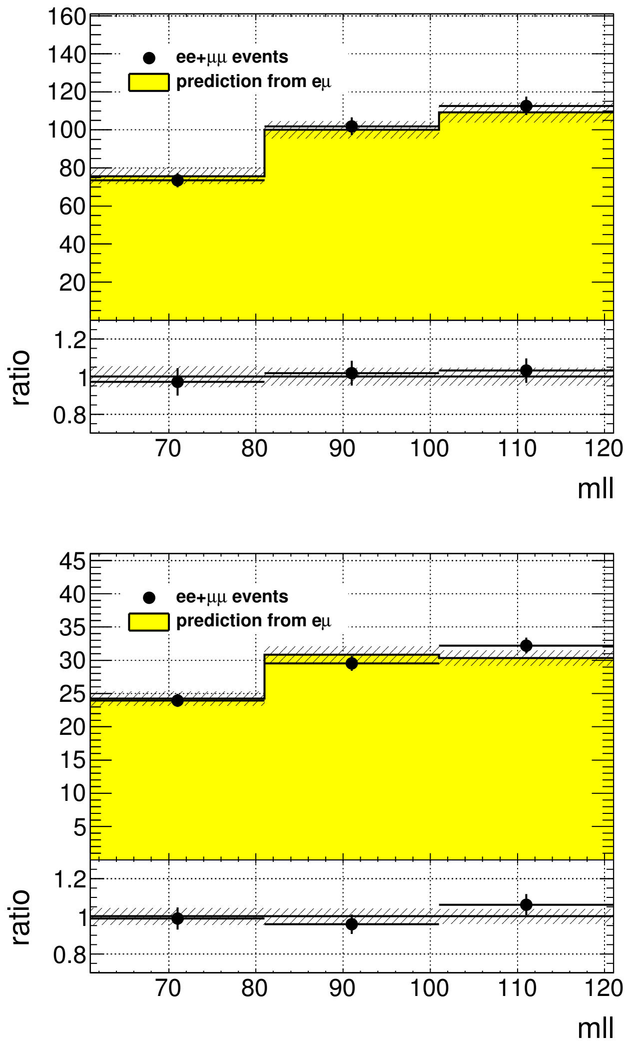

Figure 27: MC closure plots of VRS (top) and SRZ (bottom). The number of events from MC (black points) is compared to the number of events predicted from the flavor symmetry method (yellow histogram). The comparison is performed before the expanded $m_{\ell\ell}$window is used to predict the on-Z bin.

A small uncertainty is added based on the statistical uncertainty on the k and α factors derived from data. These factors are measured in many different bins (see, for example, the different measurements of k in Figure 28), and as a consequence, some bins can have very large statistical uncertainties. To assess the uncertainty on the total estimate, each measurement of these factors is varied by its uncertainty in order to produce the maximum and minimum possible prediction. This error is symmetrized, and the resulting change in the prediction is included in Table 13.

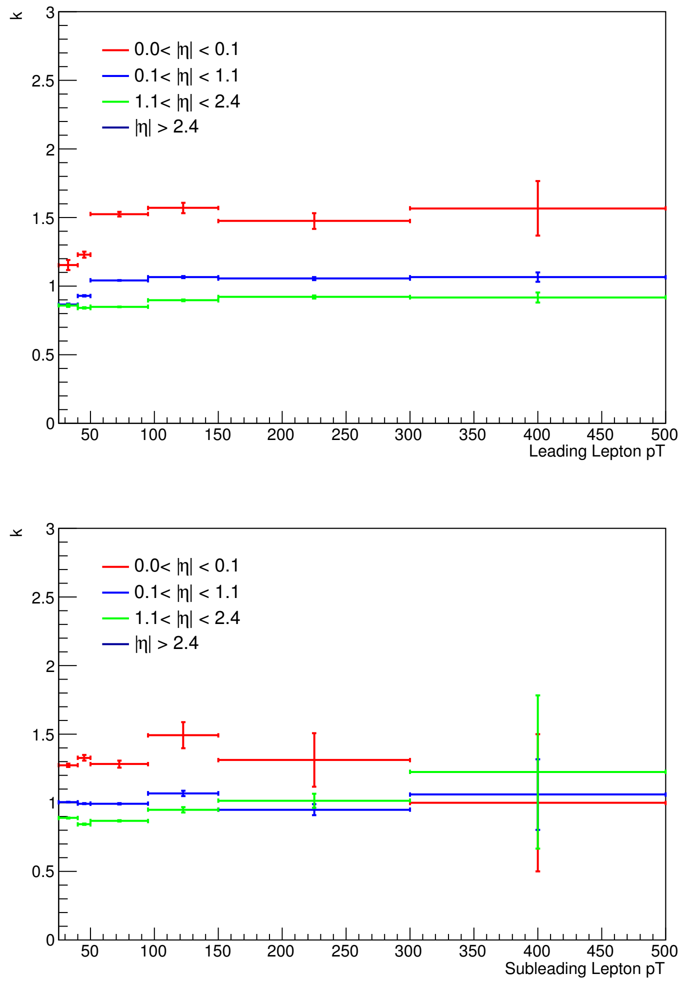

Figure 28: Measurements of k, the ratio of electron to muon events, in bins of p_T and η. On the top is the measurements indexed by the leading lepton, while the measurements indexed by the subleading lepton are on the bottom. These efficiencies are for the 2016 dataset.

The next uncertainty considers a potential bias in the way the α factors are calculated. Because they are derived from data, there is already trigger dependence in data collection (only events passing a trigger are stored) and further dependences is introduced by the use of the "dAOD" data format. This is short for derived Analysis Object Data (AOD), and they provide smaller, more efficient versions of the complete ATLAS datasets. These dAODs are designed with specific analyses in mind, filtering on the triggers and objects required by the analyses. As a consequence, there are explicit requirements that lepton or $E_{\mathrm{T}}^{\mathrm{miss}}$ triggers are passed before events are included in the dAODs used by this analysis. These requirements mean that the trigger efficiencies calculated from these samples do not include all possible events, and will have artificially high values. However, because the ratio of trigger efficiencies is the quantity needed for this analysis (see Equation 21), this will only bias the prediction if the different channels are differently impacted by the trigger preselection.

Calculating the FS prediction's dependence on these biases requires the use of MC. With a generated MC sample, there is no trigger dependence, so an unskimmed sample can be compared to a typical MC dAOD to identify the effect of the skimming. Figure 29 shows a comparison of the α factors calculated for different bins in $E_{\mathrm{T}}^{\mathrm{miss}}$ from the nominal source, data, as well as these two MC sources. A $E_{\mathrm{T}}^{\mathrm{miss}}$ dependence would be the most likely bias between the two MC-derived α factors because $E_{\mathrm{T}}^{\mathrm{miss}}$ triggers are the only triggers besides lepton triggers that will allow an event to be accepted into the dAOD used by this analysis. Though there is some difference between the data-derived α and those taken from MC, it is clear from this plot that there is very little dependence on the choice of an unskimmed or skimmed sample. The actual calculation of the uncertainty is performed by repeating the flavor symmetric method in MC with each of the two α factors and observing the difference between the estimates.

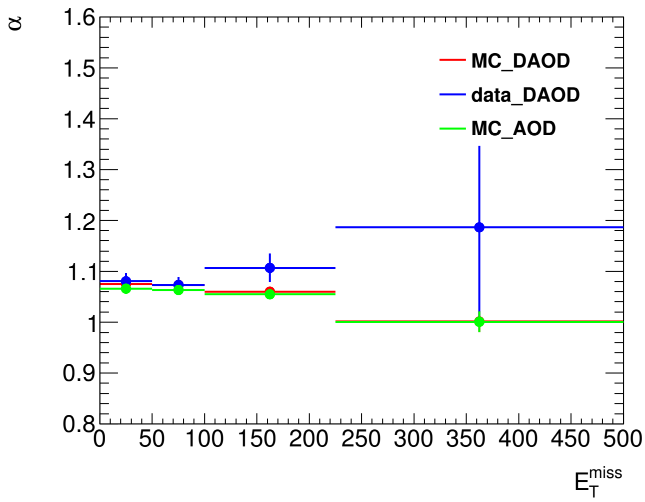

Figure 29: α, the trigger efficiency ratio, calculated as a function of $E_{\mathrm{T}}^{\mathrm{miss}}$ from three different sources: data, the usual skimmed $t\bar{t}$ MC, and an unskimmed $t\bar{t}$ MC.

The last uncertainty relates to the main MC dependence of the method - the $m_{\ell\ell}$shape of the FS background. A correction factor is taken from MC in order to account for the $m_{\ell\ell}$widening, and the accuracy of that factor must be checked. Its shape is compared to that of data in region similar to VR-FS, but with an H_T cut lowered to 300 GeVto increase statistics. The difference between the fraction of events on the Z mass peak in data and MC in this region is taken as a systematic uncertainty. To confirm that using this lowered H_T cut still gives a valid answer, the fractions are compared as a function of H_T in Figure 30. In these plots, especially in the higher-statistics 2016 plot, it is clear both that the data and MC agree very well and that there is no strong H_T dependence.

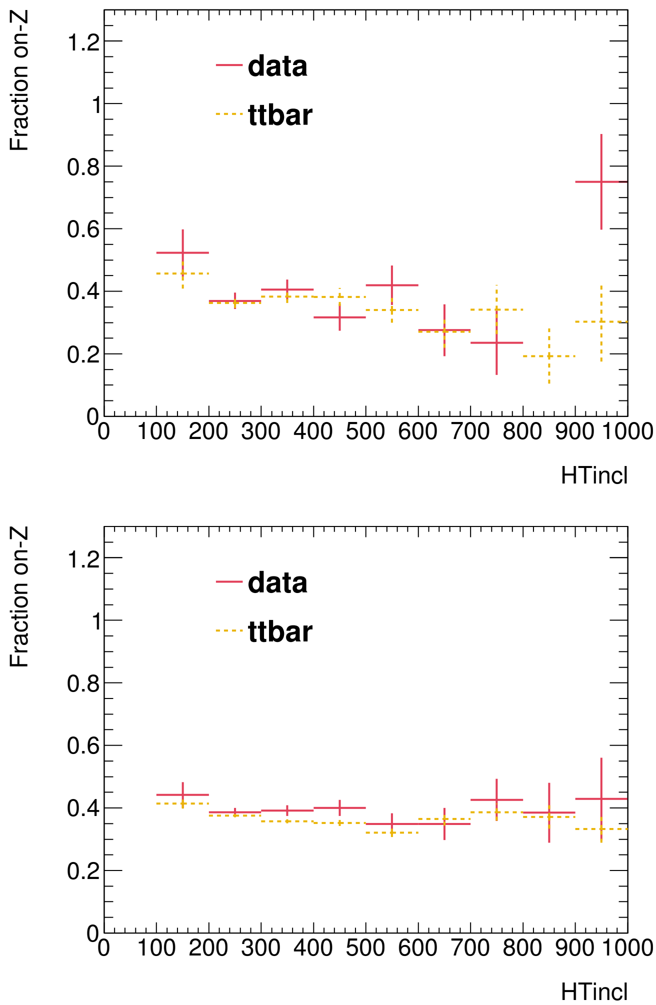

Figure 30: Plots of the fraction of on-Z events with a VR-FS-like selection as a function of H_T. The top figure shows 2015 data and MC while the bottom figure shows the same for 2016.

These uncertainties are each calculated independently for the two datasets then added. Statistical uncertainties, including the MC closure statistical uncertainties and the k and α uncertainties, are added in quadrature between the two years. Uncertainties that are more likely to be correlated, such as the difference between the two estimates in MC closure and the dependence on using a dAOD to calculate trigger efficiencies, are added linearly. The total uncertainty is about 12% of the nominal prediction in the signal region and about 9% in the validation region.

11.1.2 *Uncertainties on the γ+jets Method*

11.1.3 *Uncertainties on the Fakes Background*

Systematic uncertainties on the fakes background are derived from a series of variations on the nominal method. Variations include scaling the real and fake efficiencies up and down by their statistical uncertainties, scaling the prompt lepton contamination in CR-fake up and down by 20%, and by requiring and vetoing b-tagged jets in CR-fake to determine the dependence on heavy flavor. Statistical uncertainties can also be large in regions with small numbers of events in the the baseline selection, such as SRZ. In other regions, the b-tagging dependence provides the largest uncertainty. The full breakdown of uncertainties for the most important regions are listed in Table 14.

Variation	SRZ	CRT	CRFS	VRFS	VRS	VRT
Nominal	0.10 ± 1.61	25.39 ± 5.35	3.73 ± 2.19	10.53 ± 3.56	3.64 ± 3.20	80.06 ± 9.80
EL F Up	0.15	30.23	3.96	10.93	3.56	92.46
EL F Down	0.06	21.80	3.52	10.18	3.54	70.07
EL R Up	0.25	26.17	3.92	11.10	4.13	82.57
EL R Down	-0.07	24.51	3.52	9.92	3.10	77.24
MU F Up	-0.20	32.48	4.77	16.41	5.25	86.48
MU F Down	0.29	20.17	2.91	7.04	2.87	70.12
MU R Up	0.13	25.67	3.78	10.66	3.81	81.18
MU R Down	0.05	25.04	3.67	10.38	3.44	78.72
Total Sys	+0.26 -0.35	+8.64 -6.39	+1.08 -0.87	+5.92 -3.56	+1.70 -0.97	+14.24 -14.42
Total Sys (%)	+261.05 -354.72	+34.01 -25.19	+29.05 -23.23	+56.22 -33.85	+46.57 -26.60	+17.78 -18.02
Real Cont. Up	0.23	20.97	3.06	8.08	3.15	68.79
Real Cont. Down	-0.01	29.67	4.38	12.95	4.16	90.23
b-jet	0.31	40.44	5.28	8.98	5.63	120.50
no b-jet	0.16	23.44	3.08	11.38	3.97	70.55
Total Sys	+0.25 -0.11	+15.65 -4.83	+1.69 -0.93	+2.56 -2.90	+2.09 -0.49	+41.71 -14.74
Total Sys (%)	+260.46 -109.06	+61.66 -19.02	+45.30 -24.85	+24.32 -27.58	+57.31 -13.35	+52.10 -18.42

Table 14: Systematic uncertainties on the fake-lepton background for on-Z regions for 2015+2016 yields. The nominal yield includes statistical uncertainty from the baseline selection in a given region. The following rows indicate the results of varying the real and fake lepton efficiencies up and down by by their statistical uncertainty. Real cont. gives an uncertainty on the the contamination of real leptons in the fake lepton efficiency. b-jet and no b-jet indicate the impact of requiring or vetoing b-tagged jets in the regions used to measure the fake efficiency.

11.2 THEORETICAL AND EXPERIMENTAL UNCERTAINTIES

Experimental uncertainties cover any detector effect or LHC condition that may not be modeled precisely correctly in MC. For each uncertainty, a standard prescription from the ATLAS experiment is followed. Uncertainties are included on the following parameters:

- Luminosity (2.9%) [1, 5]
- Jet energy scale [8]
- Jet energy resolution [8]
- Jet vertex tagging
- Heavy flavor tagging
- $E_{\mathrm{T}}^{\mathrm{miss}}$ soft term [7]
- e/μ momentum scale
- e/μ trigger, reconstruction, and identification efficiencies
- Pileup

These uncertainties are applied to all MC samples used in the analysis. This includes signal models, diboson and rare top samples for the nominal estimate, and all backgrounds taken from MC in the sideband fit.

Theoretical uncertainties include cross-section uncertainties, scale uncertainties, and PDF uncertainties. For the diboson samples, the scale uncertainties, given in Table 15 and calculated by varying each scale up and down by a factor of two, are combined with a 6% cross-section uncertainty and a generator uncertainty obtained by comparing Powheg and Sherpa MC yields. The generator uncertainty, shown in Table 16, is dominant in most regions. Rare top processes are given a 13% PDF and scale variation uncertainty [18] and a 22% cross section uncertainty [26, 33, 40].

Signal models have both the central value and uncertainty on cross-sections taken from an envelope of predictions using different scales and PDF sets [37]. The signal processes are calculated at Next-to-Leading-Logarithmic Accuracy (NLO+NLL), meaning they are calculated at next-to-leading order in the strong coupling constant, with additional terms from next-to-leading-logarithmic resummation of soft gluon emission [19–21, 38, 39].

11.3 IMPACT OF UNCERTAINTIES ON THE SIGNAL REGION

The breakdown of each major uncertainty's contribution to the total uncertainty in SRZ is shown in Table 17. The dominant uncertainty is the diboson generator uncertainty, followed by the statistical uncertainty from the FS background. Uncertainties smaller than 1% are not shown in the table.

$VV \to ll\nu\nu$ Samples							
	SRZ	VRS	CRT	VRT	VRWZ	VRZZ	VR3L
resummation	0.07	0.03	0.01	0.02	0.00	0.00	0.00
renormalization	0.13	0.17	0.16	0.22	0.00	0.00	0.00
factorization	0.01	0.01	0.01	0.03	0.00	0.00	0.00
total	0.15	0.17	0.16	0.22	0.00	0.00	0.00
$WZ \to lll\nu$ Samples							
	SRZ	VRS	CRT	VRT	VRWZ	VRZZ	VR3L
resummation	0.07	0.05	0.13	0.08	0.02	0.00	0.01
renormalization	0.26	0.20	0.28	0.21	0.07	0.00	0.18
factorization	0.04	0.04	0.02	0.06	0.01	0.00	0.02
total	0.28	0.21	0.31	0.23	0.07	0.00	0.18
$ZZ \to llll$ Samples							
	SRZ	VRS	CRT	VRT	VRWZ	VRZZ	VR3L
resummation	0.27	1.07	0.01	0.01	0.06	0.01	0.53
renormalization	0.28	0.26	0.30	0.60	0.07	0.04	0.14
factorization	0.27	0.25	0.30	0.58	0.13	0.02	0.16
total	0.48	1.13	0.43	0.84	0.16	0.05	0.57

Table 15: Fractional uncertainties of dibosons in signal and validation regions from Sherpa scale variations.

Region	Sherpa Events/fb^{-1}	Sherpa Events	Powheg Events/fb^{-1}	Powheg Events	% Difference
WZ Samples					
SRZ+VRZ	5.219	76.722	3.286	48.300	37.046
CRT+VRT	1.060	15.583	0.742	10.913	29.970
WW/ZZ Samples					
SRZ+VRZ	1.921	28.244	0.685	10.070	71.424
CRT+VRT	6.281	92.332	3.142	46.188	55.474

Table 16: Comparison of yields in on-Z and off-Z regions in Sherpa and Powheg diboson MC at 14.7 fb^{-1}.

Source	Relative systematic uncertainty [%]
	SRZ
Total systematic uncertainty	17
WZ/ZZ generator uncertainty	13
Flavour symmetry (statistical)	7
WZ/ZZ scale uncertainty	6
$Z/\gamma^* +$ jets (systematic)	4
Flavour symmetry (systematic)	3
$Z/\gamma^* +$ jets (statistical)	2
Fake-leptons	1

Table 17: Overview of the dominant sources of systematic uncertainty on the total background estimate in the signal regions. The values shown are relative to the total background estimate, shown in %.

12 RESULTS

13 INTERPRETATIONS

Part V

CONCLUSIONS

This section presents conclusions and an outlook for future work.

14 CONCLUSIONS

15 OUTLOOK

Part VI

APPENDIX

A APPENDIX TEST

Aliquam lectus. Vivamus leo. Quisque ornare tellus ullamcorper nulla. Mauris porttitor pharetra tortor. Sed fringilla justo sed mauris. Mauris tellus. Sed non leo. Nullam elementum, magna in cursus sodales, augue est scelerisque sapien, venenatis congue nulla arcu et pede. Ut suscipit enim vel sapien. Donec congue. Maecenas urna mi, suscipit in, placerat ut, vestibulum ut, massa. Fusce ultrices nulla et nisl.

Etiam ac leo a risus tristique nonummy. Donec dignissim tincidunt nulla. Vestibulum rhoncus molestie odio. Sed lobortis, justo et pretium lobortis, mauris turpis condimentum augue, nec ultricies nibh arcu pretium enim. Nunc purus neque, placerat id, imperdiet sed, pellentesque nec, nisl. Vestibulum imperdiet neque non sem accumsan laoreet. In hac habitasse platea dictumst. Etiam condimentum facilisis libero. Suspendisse in elit quis nisl aliquam dapibus. Pellentesque auctor sapien. Sed egestas sapien nec lectus. Pellentesque vel dui vel neque bibendum viverra. Aliquam porttitor nisl nec pede. Proin mattis libero vel turpis. Donec rutrum mauris et libero. Proin euismod porta felis. Nam lobortis, metus quis elementum commodo, nunc lectus elementum mauris, eget vulputate ligula tellus eu neque. Vivamus eu dolor.

A.1 APPENDIX SECTION TEST

Nulla in ipsum. Praesent eros nulla, congue vitae, euismod ut, commodo a, wisi. Pellentesque habitant morbi tristique senectus et netus et malesuada fames ac turpis egestas. Aenean nonummy magna non leo. Sed felis erat, ullamcorper in, dictum non, ultricies ut, lectus. Proin vel arcu a odio lobortis euismod. Vestibulum ante ipsum primis in faucibus orci luctus et ultrices posuere cubilia Curae; Proin ut est. Aliquam odio. Pellentesque massa turpis, cursus eu, euismod nec, tempor congue, nulla. Duis viverra gravida mauris. Cras tincidunt. Curabitur eros ligula, varius ut, pulvinar in, cursus faucibus, augue.

More dummy text

Nulla mattis luctus nulla. Duis commodo velit at leo. Aliquam vulputate magna et leo. Nam vestibulum ullamcorper leo. Vestibulum condimentum rutrum mauris. Donec id mauris. Morbi molestie justo et pede. Vivamus eget turpis sed nisl cursus tempor. Curabitur mollis sapien condimentum nunc. In wisi nisl, malesuada at, dignissim sit amet, lobortis in, odio. Aenean consequat arcu a ante. Pellentesque porta elit sit amet orci. Etiam at turpis nec elit ultricies imperdiet. Nulla facilisi. In hac habitasse platea dictumst. Suspendisse

LABITUR BONORUM PRI NO	QUE VISTA	HUMAN
fastidii ea ius	germano	demonstratea
suscipit instructior	titulo	personas
quaestio philosophia	facto	demonstrated

Table 18: Autem usu id.

viverra aliquam risus. Nullam pede justo, molestie nonummy, scelerisque eu, facilisis vel, arcu.

A.2 ANOTHER APPENDIX SECTION TEST

Curabitur tellus magna, porttitor a, commodo a, commodo in, tortor. Donec interdum. Praesent scelerisque. Maecenas posuere sodales odio. Vivamus metus lacus, varius quis, imperdiet quis, rhoncus a, turpis. Etiam ligula arcu, elementum a, venenatis quis, sollicitudin sed, metus. Donec nunc pede, tincidunt in, venenatis vitae, faucibus vel, nibh. Pellentesque wisi. Nullam malesuada. Morbi ut tellus ut pede tincidunt porta. Lorem ipsum dolor sit amet, consectetuer adipiscing elit. Etiam congue neque id dolor.

Donec et nisl at wisi luctus bibendum. Nam interdum tellus ac libero. Sed sem justo, laoreet vitae, fringilla at, adipiscing ut, nibh. Maecenas non sem quis tortor eleifend fermentum. Etiam id tortor ac mauris porta vulputate. Integer porta neque vitae massa. Maecenas tempus libero a libero posuere dictum. Vestibulum ante ipsum primis in faucibus orci luctus et ultrices posuere cubilia Curae; Aenean quis mauris sed elit commodo placerat. Class aptent taciti sociosqu ad litora torquent per conubia nostra, per inceptos hymenaeos. Vivamus rhoncus tincidunt libero. Etiam elementum pretium justo. Vivamus est. Morbi a tellus eget pede tristique commodo. Nulla nisl. Vestibulum sed nisl eu sapien cursus rutrum.

There is also a useless Pascal listing below: Listing 1.

Listing 1: A floating example (listings manual)

```
for i:=maxint downto 0 do
begin
{ do nothing }
end;
```

[1] ATLAS Collaboration. "Luminosity determination in pp collisions at $\sqrt{s} = 8$ TeV using the ATLAS detector at the LHC." In: *to be submited to Eur. Phys. J. C* ().

[2] ATLAS Collaboration. "The ATLAS Experiment at the CERN Large Hadron Collider." In: *JINST* 3 (2008), S08003. DOI: 10.1088/1748-0221/3/08/S08003.

[3] ATLAS Collaboration. *Search for physics beyond the Standard Model in events with a Z boson and large missing transverse momentum using $\sqrt{s} = 7$ TeV pp collisions from the LHC with the ATLAS detector*. ATLAS-CONF-2012-046. 2012. URL: http://cdsweb.cern.ch/record/1448222.

[4] ATLAS Collaboration. *Search for supersymmetry in final states with jets, missing transverse momentum and a Z boson at $\sqrt{s} = 8$ TeV with the ATLAS detector*. ATLAS-CONF-2012-152. 2012. URL: http://cds.cern.ch/record/1493491.

[5] ATLAS Collaboration. "Improved luminosity determination in pp collisions at $\sqrt{s} = 7$ TeV using the ATLAS detector at the LHC." In: *Eur. Phys. J. C* 73 (2013), p. 2518. DOI: 10.1140/epjc/s10052-013-2518-3. arXiv: 1302.4393 [hep-ex].

[6] ATLAS Collaboration. "A neural network clustering algorithm for the ATLAS silicon pixel detector." In: *JINST* 9 (2014), P09009. DOI: 10.1088/1748-0221/9/09/P09009. arXiv: 1406.7690 [hep-ex].

[7] ATLAS Collaboration. *Expected performance of missing transverse momentum reconstruction for the ATLAS detector at $\sqrt{s} = 13$ TeV*. ATL-PHYS-PUB-2015-023. 2015. URL: http://cds.cern.ch/record/2037700.

[8] ATLAS Collaboration. *Jet Calibration and Systematic Uncertainties for Jets Reconstructed in the ATLAS Detector at $\sqrt{s} = 13$ TeV*. ATL-PHYS-PUB-2015-015. 2015. URL: http://cds.cern.ch/record/2037613.

[9] ATLAS Collaboration. *Measurement of performance of the pixel neural network clustering algorithm of the ATLAS experiment at $\sqrt{s} = 13$ TeV*. ATL-PHYS-PUB-2015-044. 2015. URL: http://cdsweb.cern.ch/record/2054921.

[10] ATLAS Collaboration. *Robustness of the Artificial Neural Network Clustering Algorithm of the ATLAS experiment*. ATL-PHYS-PUB-2015-052. 2015. URL: http://cdsweb.cern.ch/record/2116350.

[11] ATLAS Collaboration. "Search for squarks and gluinos in events with isolated leptons, jets and missing transverse momentum at $\sqrt{s} = 8$ TeV with the ATLAS detector." In: *JHEP* 1504 (2015), p. 116. DOI: 10.1007/JHEP04(2015)116. arXiv: 1501.03555 [hep-ex].

[12] ATLAS Collaboration. "Search for supersymmetry in events containing a same-flavour opposite-sign dilepton pair, jets, and large missing transverse momentum in $\sqrt{s} = 8$ TeV pp collisions with the ATLAS detector." In: *Eur. Phys. J. C* 75 (2015), p. 318. DOI: 10.1140/epjc/s10052-015-3518-2. arXiv: 1503.03290 [hep-ex].

[13] ATLAS Collaboration. "Measurement of the differential cross-section of highly boosted top quarks as a function of their transverse momentum in $\sqrt{s} = 8$ TeV proton-proton collisions using the ATLAS detector." In: *Phys. Rev. D* 93.3 (2016), p. 032009. DOI: 10.1103/PhysRevD.93.032009. arXiv: 1510.03818 [hep-ex].

[14] ATLAS Collaboration. *Modelling of the $t\bar{t}H$ and $t\bar{t}V$ $(V = W, Z)$ processes for $\sqrt{s} = 13$ TeV ATLAS analyses*. ATL-PHYS-PUB-2016-005. 2016. URL: http://cds.cern.ch/record/2120826.

[15] ATLAS Collaboration. *Monte Carlo Generators for the Production of a W or Z/γ^* Boson in Association with Jets at ATLAS in Run 2*. ATL-PHYS-PUB-2016-003. 2016. URL: http://cds.cern.ch/record/2120133.

[16] ATLAS Collaboration. *Multi-Boson Simulation for 13 TeV ATLAS Analyses*. ATL-PHYS-PUB-2016-002. 2016. URL: http://cds.cern.ch/record/2119986.

[17] ATLAS Collaboration. *Simulation of top quark production for the ATLAS experiment at $\sqrt{s} = 13$ TeV*. ATL-PHYS-PUB-2016-004. 2016. URL: http://cds.cern.ch/record/2120417.

[18] J. Alwall, R. Frederix, S. Frixione, V. Hirschi, F. Maltoni, O. Mattelaer, H. S. Shao, T. Stelzer, P. Torrielli, and M. Zaro. "The automated computation of tree-level and next-to-leading order differential cross sections, and their matching to parton shower simulations." In: *JHEP* 07 (2014), p. 079. DOI: 10.1007/JHEP07(2014)079. arXiv: 1405.0301 [hep-ph].

[19] W. Beenakker, R. Höpker, M. Spira, and P.M. Zerwas. "Squark and gluino production at hadron colliders." In: *Nucl. Phys. B* 492 (1997), pp. 51–103. DOI: 10.1016/S0550-3213(97)00084-9. arXiv: hep-ph/9610490 [hep-ph].

[20] W. Beenakker et al. "Soft-gluon resummation for squark and gluino hadroproduction." In: *JHEP* 0912 (2009), p. 041. DOI: 10.1088/1126-6708/2009/12/041. arXiv: 0909.4418 [hep-ph].

[21] W. Beenakker et al. "Squark and gluino hadroproduction." In: *Int. J. Mod. Phys. A* 26 (2011), pp. 2637–2664. DOI: 10.1142/S0217751X11053560. arXiv: 1105.1110 [hep-ph].

[22] C. P. Burgess and G. D. Moore. *The standard model: A primer*. Cambridge University Press, 2006. ISBN: 9780511254857, 9781107404267, 9780521860369.

[23] CMS Collaboration. "Search for physics beyond the standard model in events with a Z boson, jets, and missing transverse energy in pp collisions at $\sqrt{s} = 7$ TeV." In: *Phys. Lett. B* 716 (2012), pp. 260–284. DOI: 10.1016/j.physletb.2012.08.026. arXiv: 1204.3774 [hep-ex].

[24] CMS Collaboration. "Measurement of the integrated and differential t-tbar production cross sections for high-pt top quarks in pp collisions at $\sqrt{s}$ = 8 TeV." In: *Phys. Rev. D* (2016). Submitted. arXiv: 1605.00116 [hep-ex].

[25] J. M. Campbell and R. K. Ellis. "An update on vector boson pair production at hadron colliders." In: *Phys. Rev. D* 60 (1999), p. 113006. arXiv: hep-ph/9905386 [hep-ph].

[26] J. M. Campbell and R. K. Ellis. "$t\bar{t}$ W production and decay at NLO." In: *JHEP* 1207 (2012), p. 052. arXiv: 1204.5678 [hep-ph].

[27] J. M. Campbell, R. K. Ellis, and C. Williams. "Vector boson pair production at the LHC." In: *JHEP* 1107 (2011), p. 018. arXiv: 1105.0020 [hep-ph].

[28] S. Catani and M. Grazzini. "An NNLO subtraction formalism in hadron collisions and its application to Higgs boson production at the LHC." In: *Phys. Rev. Lett.* 98 (2007), p. 222002. arXiv: hep-ph/0703012 [hep-ph].

[29] S. Catani, L. Cieri, G. Ferrera, D. de Florian, and M. Grazzini. "Vector boson production at hadron colliders: a fully exclusive QCD calculation at NNLO." In: *Phys. Rev. Lett.* 103 (2009), p. 082001. arXiv: 0903.2120 [hep-ph].

[30] M. Czakon, P. Fiedler, and A. Mitov. "Total Top-Quark Pair-Production Cross Section at Hadron Colliders Through $O(\alpha_s^4)$." In: *Phys. Rev. Lett.* 110 (2013), p. 252004. arXiv: 1303.6254 [hep-ph].

[31] M. Czakon and A. Mitov. "Top++: A Program for the Calculation of the Top-Pair Cross-Section at Hadron Colliders." In: *Comput. Phys. Commun.* 185 (2014), p. 2930. DOI: 10.1016/j.cpc.2014.06.021. arXiv: 1112.5675 [hep-ph].

[32] D. Galbraith.

[33] M. V. Garzelli, A. Kardos, C. G. Papadopoulos, and Z. Trocsanyi. "t $\bar{t}$ W^{+-} and t $\bar{t}$ Z Hadroproduction at NLO accuracy in QCD with Parton Shower and Hadronization effects." In: *JHEP* 11 (2012), p. 056. DOI: 10.1007/JHEP11(2012)056. arXiv: 1208.2665 [hep-ph].

[34] David J Griffiths. *Introduction to elementary particles; 2nd rev. version*. Physics textbook. New York, NY: Wiley, 2008. URL: https://cds.cern.ch/record/111880.

[35] Huang, Qing-Guo, Wang, Ke, and Wang, Sai. "Constraints on the neutrino mass and mass hierarchy from cosmological observations." In: *Eur. Phys. J. C* 76.9 (2016), p. 489. DOI: 10.1140/epjc/s10052-016-4334-z. URL: http://dx.doi.org/10.1140/epjc/s10052-016-4334-z.

[36] N. Kidonakis. "Two-loop soft anomalous dimensions for single top quark associated production with a W^- or H^-." In: *Phys. Rev. D* 82 (2010), p. 054018. DOI: 10.1103/PhysRevD.82.054018. arXiv: 1005.4451 [hep-ph].

[37] Michael Kramer et al. *Supersymmetry production cross sections in pp collisions at $\sqrt{s} = 7$ TeV*. 2012. arXiv: 1206.2892 [hep-ph].

[38] A. Kulesza and L. Motyka. "Soft gluon resummation for the production of gluino-gluino and squark-antisquark pairs at the LHC." In: *Phys. Rev. D* 80 (2009), p. 095004. DOI: 10.1103/PhysRevD.80.095004. arXiv: 0905.4749 [hep-ph].

[39] A. Kulesza and L. Motyka. "Threshold resummation for squark-antisquark and gluino-pair production at the LHC." In: *Phys. Rev. Lett.* 102 (2009), p. 111802. DOI: 10.1103/PhysRevLett.102.111802. arXiv: 0807.2405 [hep-ph].

[40] A. Lazopoulos, T. McElmurry, K. Melnikov, and F. Petriello. "Next-to-leading order QCD corrections to $t\bar{t}Z$ production at the LHC." In: *Phys. Lett. B* 666 (2008), p. 62. arXiv: 0804.2220 [hep-ph].

[41] A. D. Martin, W. J. Stirling, R. S. Thorne, and G. Watt. "Parton distributions for the LHC." In: (2009). DOI: 10.1140/epjc/s10052-009-1072-5. eprint: arXiv:0901.0002.

[42] Johan Messchendorp. "Physics with Charmonium – A few recent highlights of BESIII." In: *PoS* Bormio2013 (2013), p. 043. arXiv: 1306.6611 [hep-ex].

[43] F. Zwicky. "Die Rotverschiebung von extragalaktischen Nebeln." In: *Helvetica Physica Acta* 6 (1933), 110–127.

[44] LHCb collaboration. "Observation of $J/\Psi p$ resonances consistent with pentaquark states in $\Lambda_b^0 \to J/\Psi K^- p$ decays." In: (2015). DOI: 10.1103/PhysRevLett.115.072001. eprint: arXiv:1507.03414.

[45] T. S. van Albada, J. N. Bahcall, K. Begeman, and R. Sancisi. "Distribution of dark matter in the spiral galaxy NGC 3198." In: *The Astrophysical Journal* 295 (Aug. 1985), pp. 305–313. DOI: 10.1086/163375.